Dynamics and mixing in jet/vortex interactions

R. Paoli*, F. Laporte*, B. Cuenot*, T. Poinsot*×

*CERFACS, 42 Avenue Gaspart Coriolis, 31057 Toulouse, France

×IMFT, Allée du Professeur Camille Soula, 31400 Toulouse, France

(March 24, 2003)

Abstract

This study describes Large Eddy Simulations (LES) of the interaction between an exhaust jet and a trailing vortex, in the near-field of an aircraft wake. Two cases are analyzed: in the first one, typical of cruise flight, the jet and the vortex axes are sufficiently well separated to study first the jet dynamics before considering its interaction with the vortex. Dynamics and mixing are controlled both by the jet diffusion and its entrainment around the vortex core. In the second case the jet partially blows in the vortex core, making the flow similar to a Batchelor vortex. The strong perturbations injected into the core cause an instability of the system which is continuously fed by the jet elements wrapping around the core. This leads to a strong decay of angular momentum and diffusion of the core. Global mixing properties, such as plume area and global mixedness evolutions, are analyzed and two applications to environmental problems are finally discussed.

I. INTRODUCTION

The interaction between aircraft wake vortices and exhaust jets is of primary interest in applications covering a wide spectrum of aerospace technology, from the characterization of the structure of persistent and hazardous trailing vortices during taking off and landing phases,[1,2] to the investigation of the impact of aircraft emissions on the atmospheric environment. The latter has been assessed in the Intergovernmental Panel on Climate Change (IPCC) special report of 1999[3], where a need was identified for further research in some key topics. Gaseous emissions like CO_2, NO_x and SO_x alter the concentration of atmospheric greenhouse gases; particles resulting from incomplete combustion like soot, trigger the formation of condensation trails (contrails), increasing artificially cloudiness and altering climate.[3,4] Besides these global effects, aircraft emissions also play a major role in the production of local pollution; indeed, gases like CO or CH_4 emitted by the engines are trapped by aircraft trailing vortices in very localized zones thus contributing to air pollution around the airports. These specific issues have been addressed by different authors, mostly in geophysical and atmospheric sciences, through *in situ* measurements[5,6] or numerical simulations with different levels of complexity.[7,8] The main intent was there to characterize the general features of the exhaust plumes diffusion, on length-scales up to hundred meters from the engine and time-scales up to minutes from the emission time.

The goal of the present work is to analyze in detail the interaction between an exhaust jet and a trailing vortex, in the near-field of an aircraft wake (Fig. 1). This is a necessary step to understand how exhaust gases expand in the atmosphere and which is the role of the vortex in the jet dynamics and mixing with ambient air, during the first seconds after the emission. At the same time, it is useful to evaluate the local effects of "single-aircraft" emissions on the atmospheric environment, and provide inputs to climate or environmental investigations.

The qualitative features of the jet/vortex interaction were illustrated by Miake-Lye *et al.*[9] who identified two distinct phases. During the first few seconds after the emission the jets

rapidly mix with ambient air (jet regime) while the vorticity shed from the wings rolls up into a pair of trailing vortices. Later on, the dynamics is dominated by the entrainment of the jets into the vortex flow (interaction regime). Only few numerical studies have addressed the specific issue of jet/wake vortex interaction. A Direct Numerical Simulation (DNS) of jet/vortex dynamics and mixing was performed by Ferreira Gago *et al.*,[10] solving sequentially the two phases described above; they observed the development of counter-rotating structures with high azimuthal vorticity where the scalar field, representing any engine exhaust gas, initially localized in the jet, concentrates. Nevertheless the very low Reynolds number assumption used in their study imposes strict limits: realistic flight Reynolds numbers are necessary to correctly predict the dispersion of exhaust gas. The work of Ferreira Gago *et al.*[10] is the natural continuation of the pioneering studies done by Jacquin and Garnier,[11] Gerz and Ehret[12] and Brunet *et al.*.[13] An interesting tentative to simulate the jet/vortex sheet interaction in a realistic aircraft flow geometry has also been done recently by Fares *et al.*[14] with a sophisticated Reynolds averaged Navier-Stokes solver, keeping, however, the intrinsic limitations of steady flow assumption.

Looking at the jet and wake vortex interaction requires previous knowledge on the generic dynamics of jets and aircraft wakes. Jet profiles are known to be unstable, with a robust instability mechanism of Kelvin-Helmoltz type. By using normal modes approach, Michalke and Herman[15] provided the exact growth rates of the instability developing spatially in an inviscid incompressible jet. Brancher[16] performed a linear analysis for the same inviscid incompressible jet developing temporally, and completed the analysis for viscous flows with spectral numerical simulations. Loiseleux *et al.*[17] and Lu and Lele[18] extended the analysis to swirling flows, respectively for jets and wakes and for mixing layers.

The characteristics of engine jets may be significantly different from the academic jet flows studied within the framework of the linear stability theory. During the take-off phase, realistic aircraft wakes may comprise supersonic jets with significant compressibility effects (see for example Freund *et al.*).[19] Heating increases axial mixing and entrainment of jets by cold external air through density gradients, as shown, for instance, by Ricou and Spalding[20]

who measured increased entrainment rates for hydrogen jets and Abramovich *et al.*[21] who measured larger axial vortex decay and mixing for low density ratios, S_ρ, between jet and air flow. Density ratio also affects jet stability: Monkewitz and Sohn[22] found that the jet becomes absolutely unstable when S_ρ is reduced below 0.72.

The wake structure of an aircraft in the near to mid-field (less than 50 spans behind the aircraft) may be different depending on the flight phase and the type of aircraft (see e.g. the reviews of Spalart[1] or Rossow).[2] The aircraft sheds a vorticity sheet at the trailing edge of the lifting surface, which rolls-up into a small number of concentrated vortices in a distance often not greater than 5 to 10 spans behind the aircraft. On cruise flight, the vorticity sheet shed by one wing essentially rolls up into a single vortex, emanating from the wing tip. For both two- or four-engine aircrafts, the jets are produced far from the initial vortex position. The complete wake is composed by a counter-rotating vortex pair in this case. In high-lift configurations the wake shed by one wing may roll up into several co- or counter-rotating vortices, depending on the flap setting. These vortices interact in the near to mid-field, which often results in the merging of the co-rotating structures and the formation of a single vortex pair in the far-field, as it is the case for cruise flight conditions. In these configurations, the jet/vortex sheet interaction is more complex than in cruise flight, since, for example, four-engine aircrafts may generate jets in the vicinity of the flap vortex. Regions of combined rotational fluid and axial velocity may be considered as swirling jets or as vortices with axial velocity, and are known to be unstable under certain conditions (Mayer and Powell[25], Hu *et al.*).[26] Characterization studies have brought detailed knowledge on the wake vortex structure in the near to mid-field (Devenport *et al.*,[27,28] Chen *et al.*[29], Jacquin *et al.*[30] and Laporte)[31] either for cruise or high-lift configurations. Stability properties of wake vortex systems in this part of the wake have been studied by means of linear stability analysis, experiments and numerical simulations. Several instability mechanisms have been evidenced (Mayer and Powell,[25] Ragab and Sreedhar,[32] Crouch,[33] Rennich and Lele,[34] Fabre and Jacquin,[35] Leweke *et al.*,[36] Fabre *et al.*,[37] Le Dizès and Laporte).[38] Nevertheless, detailed analyses of the jet/vortex dynamics in the wake are still missing.

As the dynamics of the jets and vortices are intrinsically highly unsteady, Large Eddy Simulation (LES) is well adapted to study all the large scale phenomena involved. The goal of this study is to use LES for the jet/vortex interaction dynamics as well as for the jet mixing characteristics, in the near-field of an aircraft. Two types of interactions are analyzed: in the first one, referred to as "entrainment case", the jet and the vortex are initially well-separated, which is always the case in cruise flight, or in particular high-lift configurations of two-engine aircrafts; in the second one, referred as "blowing case", the jet blows inside the vortex core and is suitable to model high lift configurations. Other configurations including jet and vortex sheet have been studied by the same authors,[39] but are not reported here for the sake of conciseness. For the entrainment case, the jet and the interaction regimes can be studied separately, following the approach described above.[9,10] The jet regime corresponds to the distance for the jet to become fully turbulent, which is less than one wingspan downstream of the aircraft, and of the same order of magnitude as the distance for wake roll-up completion (formation of a circular wing-tip vortex). During the jet regime, the interaction is weak, and the wake is composed by a single and well-formed vortex when the interaction starts. This allows a simplification of the initial flow conditions without taking into account the roll-up phase. In order to spare computational time and memory, the flow is assumed to be locally parallel, and developing in a temporal mode.[16,40,41] These two last hypotheses are discussed later in the paper. The paper is organized as follows. Section II is dedicated to the formulation of the governing equations, the LES approach and subgrid-scale modeling, the numerical methods and the physical assumptions. The dynamics and mixing of the interaction are analyzed in Sections III and IV, for the the entrainment and blowing cases, respectively. Applications to environmental problems are discussed in Section V, respectively, the evaluation of the dilution of a general exhaust gas by wake dispersion, and the prediction of the formation of condensation trails. Some concluding remarks are given in Section VI about the main outcomes of the present study.

II. GOVERNING EQUATIONS, MODELING AND PHYSICAL ASSUMPTIONS

The dimensionless formulation of the 3D compressible Navier-Stokes equations reads

$$\frac{\partial \rho}{\partial t} + \frac{\partial (\rho u_j)}{\partial x_j} = 0 \tag{1}$$

$$\frac{\partial (\rho u_i)}{\partial t} + \frac{\partial (\rho u_i u_j)}{\partial x_j} + \frac{\partial p}{\partial x_i} = \frac{1}{Re} \frac{\partial \tau_{ij}}{\partial x_j} \tag{2}$$

$$\frac{\partial (\rho E)}{\partial t} + \frac{\partial [(\rho E + p) u_j]}{\partial x_j} = \frac{1}{Re} \frac{\partial (u_i \tau_{ij})}{\partial x_j} - \frac{1}{Re\, Pr} C_p \frac{\partial q_j}{\partial x_j} \tag{3}$$

where the non-dimensional variables are: the density ρ, the velocity vector $(u_1, u_2, u_3)^T$, the pressure p, the total energy E, the heat flux vector $(q_1, q_2, q_3)^T$ given by Fourier's law, and the shear stress tensor τ_{ij}. The C_p coefficient is the specific heat at constant pressure. The non-dimensional variables are defined as the local dimensional variables divided by a reference variable or a combination of the reference variables. The reference variables are: the density ρ_{ref}, the velocity a_{ref}, the pressure p_{ref}, the length l_{ref}, the temperature T_{ref}, the dynamic viscosity μ_{ref} and the specific heat $C_{p,ref}$. The reference Reynolds number is $Re = a_{ref}\, l_{ref}/(\mu_{ref}/\rho_{ref})$ while Pr stands for the Prandtl number. Mixing is studied through the passive scalar transport equation:

$$\frac{\partial (\rho Y)}{\partial t} + \frac{\partial (\rho Y u_j)}{\partial x_j} = \frac{1}{Re\, Sc} \frac{\partial}{\partial x_j} \left(\mu \frac{\partial Y}{\partial x_j} \right) \tag{4}$$

where Y is the passive scalar mass fraction, and Sc denotes the Schmidt number. In the present simulations $Pr = Sc = 0.75$ which gives a Lewis number $Le = Sc/Pr = 1$.

A. LES approach and subgrid-scale model description

In the LES approach the previous equations are filtered spatially, so that any variable $\phi(x)$ may be decomposed into a resolved (or large scale) part $\overline{\phi(x)}$ and a non-resolved (or subgrid-scale) part $\phi''(x)$, with $\phi(x) = \overline{\phi(x)} + \phi''(x)$. This procedure may be obtained by a convolution integral of the variable with a filter function depending on a filter width Δ. Practically, the filter width is simply given by the computational mesh cell size Δ_x. For

compressible flows, Favre-filtered variables, defined as $\phi(x) = \tilde{\phi}(x) + \phi'(x)$, with $\tilde{\phi} = \overline{\rho\phi}/\overline{\rho}$ are used. The dimensionless Favre-filtered equations are:

$$\frac{\partial \overline{\rho}}{\partial t} + \frac{\partial(\overline{\rho}\tilde{u}_j)}{\partial x_j} = 0 \tag{5}$$

$$\frac{\partial(\overline{\rho}\tilde{u}_i)}{\partial t} + \frac{\partial(\overline{\rho}\tilde{u}_i\tilde{u}_j)}{\partial x_j} + \frac{\partial \overline{p}}{\partial x_i} = \frac{1}{Re}\frac{\partial \tilde{\tau}_{ij}}{\partial x_j} + \frac{\partial \sigma_{ij}}{\partial x_j} \tag{6}$$

$$\frac{\partial(\overline{\rho}\tilde{E})}{\partial t} + \frac{\partial[(\overline{\rho}\tilde{E} + \overline{p})\tilde{u}_j]}{\partial x_j} = \frac{1}{Re}\frac{\partial \tilde{\tau}_{ij}\tilde{u}_i}{\partial x_j} + \frac{\partial \sigma_{ij}\tilde{u}_i}{\partial x_j} - \frac{1}{Re\,Pr}C_p\frac{\partial \tilde{q}_j}{\partial x_j} - \frac{\partial Q_j}{\partial x_j} \tag{7}$$

where the subgrid-scale (SGS) stress tensor $\sigma_{ij} = -(\overline{\rho u_i u_j} - \overline{\rho}\tilde{u}_i\tilde{u}_j)$, and the SGS heat flux $Q_j = \overline{\rho C_p T u_j} - \overline{\rho} C_p \tilde{T}\tilde{u}_j$ are to be modeled, and where the following classical approximations (see Erlebacher *et al.*)[42] have been made:

- The Favre-filtered shear stress tensor is identified with the filtered shear stress tensor
- The Favre-filtered heat flux is identified with the filtered heat flux
- The filtered kinetic energy term $\overline{\rho K u_j}$ in the energy equation is approximated by $\overline{\rho}\tilde{K}\tilde{u}_j - \sigma_{ij}\tilde{u}_j$, where $K = 1/2\, u_i u_i$ is the kinetic energy.

The Favre-filtered passive scalar equation is:

$$\frac{\partial(\overline{\rho}\tilde{Y})}{\partial t} + \frac{\partial(\overline{\rho}\tilde{Y}\tilde{u}_j)}{\partial x_j} = \frac{1}{Re\,Sc}\frac{\partial}{\partial x_j}\left(\mu\frac{\partial \tilde{Y}}{\partial x_j}\right) + \frac{\partial \xi_j}{\partial x_j} \tag{8}$$

The SGS momentum, σ_{ij}, the SGS heat flux, Q_j, and the SGS scalar flux, ξ_j, are modeled through subgrid-scale eddy-viscosity concept:

$$\sigma_{ij} - \frac{1}{3}\sigma_{kk}\delta_{ij} = -2\mu_{sgs}\Big(\tilde{S}_{ij} - \frac{1}{3}\delta_{ij}\tilde{S}_{kk}\Big) \tag{9}$$

$$Q_j = -\frac{\mu_{sgs}\,C_p}{Pr_t}\frac{\partial \Theta}{\partial x_j} \tag{10}$$

$$\xi_j = -\frac{\mu_{sgs}}{Sc_t}\frac{\partial \tilde{Y}}{\partial x_j} \tag{11}$$

where μ_{sgs} is the SGS dynamic viscosity, $\tilde{S}_{ij}$ is the large scale strain rate tensor and Sc_t is the turbulent Schmidt number; while Pr_t is the turbulent Prandtl number, defining the modified temperature $\Theta = \tilde{T} - \frac{1}{2\overline{\rho}C_v}\sigma_{kk}$, where C_v is the specific heat at constant volume. The SGS viscosity model is based on the Structure Function model (Métais & Lesieur)[43]

initially developed in spectral space (effective viscosity model) and then transposed into the physical space. The expression of the Structure Function is

$$\overline{F}_2(\vec{x},\Delta,t) = \langle \| \vec{\tilde{u}}(\vec{x}+\vec{r},t) - \vec{\tilde{u}}(\vec{x},t) \| \rangle_{\|\vec{r}\|=\Delta} \tag{12}$$

where Δ is the cutoff length, and where $\langle\rangle$ denotes spatial averaging, here over the sphere of radius Δ. As the information brought by the model is local in space, it leads to a poor estimation of the kinetic energy at the cutoff, which may be improved by a suitable filtering,[44] in order to remove the influence of the large scales on the SGS viscosity. The procedure defined by Ducros *et al.*[44] is to apply (possibly n times) a discrete Laplacian high-pass filter to the velocity field before calculating the Structure Function. The optimum value of n found by Ducros *et al.*[44] for their simulations is $n = 3$. This value has also been used here. Finally, the Filtered Structure Function model reads:

$$\nu_{sgs} = \overline{\rho}\,\mu_{sgs} = \nu_{sgs}(\vec{x},\Delta,t) = \alpha^{(n)}\Delta\sqrt{\overline{F_2}^{(n)}(\vec{x},\Delta,t)} \tag{13}$$

where the superscript (n) indicates that the filter has been applied n times. The value of α used here is $\alpha^{(3)} = 0.00084$. The Structure Function model formulation of Métais & Lesieur[43] in the spectral space insures that the SGS viscosity vanishes when there is no energy at the cutoff wavelength. This property is particularly important for the simulation of transitional flows as those of interest in the present paper. In particular, recent LES of the elliptical stability of a vortex pair,[38] have shown that the model predicts the correct evolution of the core radius during its transition to turbulence, at high Reynolds number $Re = 5\,10^5$.

B. Numerical method

The numerical code[46–48] used for this study, is a parallel, three-dimensional, finite differences Navier-Stokes solver. The space discretization is performed by a sixth-order compact scheme[49] for both convective and viscous terms. Time integration is performed by means of a three-stage Runge-Kutta method.

Periodic boundary conditions are used along the jet/vortex axis z and non-reflecting boundary conditions on the $x-y$ directions (Fig. 2). The latter are treated according to the characteristic approach developed by Poinsot and Lele,[50] with a pressure relaxation term on the incoming characteristic waves in order to maintain the pressure close to the free-stream value. Special care has also been taken to isolate the interior of the domain from the non-reflecting boundaries by placing them far enough and by inserting a buffer zone (five grid points in the present calculations) where the turbulent viscosity was artificially increased with an exponential law.

C. Physical assumptions

The first assumption is that the temporal evolution of the flow is a good representation of its spatial evolution. This is based on the assumption of a locally parallel flow, which means that the gradients of the mean flow in the axial direction are neglected over the short distance corresponding to the axial dimension of the simulation domain. Instabilities developing in the simulated flow are automatically of convective nature, and we may not capture absolute instabilities.[16] Nevertheless, the Kelvin-Helmoltz instability developing in jet flows has been shown to be convective (see Brancher[16] and references therein), and the 3D temporal simulation approach has been validated for academic flows, as mixing layers or jets.[16,26,51]

The second physical hypothesis, used in Sec. III, is to assume that the flow evolution can be split into two sequential phases: the jet phase, where the jet is simulated alone, and the interaction phase, where a vortex is inserted in the turbulent jet flow. As mentioned in the Introduction, this assumption is not straightforward looking at the complex flow behind an aircraft, since the engine jets interact with the vortex sheet shed by the wing. In cruise flight the vorticity sheet shed by one wing rolls-up into a single concentrated and almost circular vortex, initially emitted at the wing tip. The distance for roll-up completion is of the order of one aircraft span, which corresponds to tens of jet exit radii. As the jet is

expected to become fully turbulent over a distance of the order of ten jet exit radii, the well-formed vortex interacts with a turbulent jet. Therefore, we assume that the jet base flow is not strongly modified (jet profile stretching) by the vortex sheet during the characteristic time scale of the jet instability. An evaluation of these time scales in our case shows that during the time taken by the jet to travel one initial jet radius (with the velocity induced by the vortex), the amplitude of the jet instability has grown approximately of a factor e. During this time, the differential effects of the vortex induced velocity on the initially axisymmetric jet profile (corrugation effects) are expected to be very weak. A maximum differential displacement of the core of the order of 3% of the jet radius is observed in the LES, validating *a posteriori* our approach.

III. ENTRAINMENT CASE

This section describes the dynamics and mixing during the jet phase (Sec. III A) and the interaction phase (Sec. III B). The Reynolds number, based on the jet radius, r_j and exit velocity, w_j, is $Re_j = 3.2\,10^6$ and the jet Mach number is $M_j = \frac{w_j}{a_{ref}} = 0.2$. Turbulent Prandtl and Schmidt numbers are the same as the laminar values, i.e., $Pr_t = Pr = 0.75$ and $Sc_t = Sc = 0.75$.

A. Jet phase

In the first phase, the computational domain has dimensions $L_x = L_y = 16r_j$ and $L_z = 6r_j$ (see sketch of Fig. 2). It consists of an equi-spaced mesh of $161 \times 161 \times 61$ nodes, giving $\Delta_x = \Delta_y = \Delta_z = 0.1r_j$ (referred to as mesh 1). We also performed simulations on a finer grid in the transversal plane, $\Delta_x = \Delta_y = 0.075r_j$ (referred to as mesh 2). The length of the axial direction was chosen according to the results obtained by the stability analysis of Michalke and Herman[15] while the transversal lengths were chosen to minimize the effects of the boundaries. The jet axial velocity is initialized as $w = w_0(1 + \epsilon\tilde{w})$ where w_0 is a *tanh* profile (r is the radial coordinate in a cross-section)

$$w_0(r) = \frac{1}{2}\left\{(w_j + w_a) - (w_j - w_a)\tanh\left[\frac{1}{4}\frac{r_j}{\theta}\left(\frac{r}{r_j} - \frac{r_j}{r}\right)\right]\right\} \tag{14}$$

Subscripts j and a indicate, respectively, exhaust jet and ambient air, while $\epsilon\tilde{w}$ is a white noise random perturbation with maximum amplitude 0.5% of the local base flow w_0, i.e. $\epsilon = 0.005$ and $||\tilde{w}|| \leq 1$. The momentum thickness θ, defined as:

$$\theta = \int_0^\infty \frac{w(r)}{w_j}\left(1 - \frac{w(r)}{w_j}\right) dr \tag{15}$$

was set equal to $r_j/\theta = 10$ which corresponds to the most unstable case in the theoretical analysis of Michalke and Herman.[15] Passive scalar is initialized as:

$$Y_0(r) = \frac{1}{2}\left\{(Y_j + Y_a) - (Y_j - Y_a)\tanh\left[\frac{1}{4}\frac{r_j}{\theta}\left(\frac{r}{r_j} - \frac{r_j}{r}\right)\right]\right\} \tag{16}$$

There is no co-flow, $w_a = 0$, and, unless specified, $Y_a = 0$ and $Y_j = 1$. All length scales and velocities are non-dimensionalized by w_j and r_j respectively. Non-dimensional time, t_j, is introduced as $t_j = t/(r_j/w_j)$.

The jet stability can be analyzed in terms of the growth rates associated to the axial wave-numbers through k_z.[16,26] The growth rate, σ_k, of a given axial Fourier mode k (associated to the axial wave-number by $k_z = 2\pi k/L_z$) is related to the corresponding Fourier coefficient of the square root of kinetic energy, $E_k^{1/2}$, by $\sigma_k \simeq \frac{d\ln(E_k^{1/2})}{dt}$ (see Laporte and Corjon).[45] They are obtained by performing discrete Fourier transforms of $E^{1/2}$ in the axial direction for each grid point (x_i, y_j) and then averaging over the transversal plane. Although the effects of white noise perturbation is to excite all axial wave-numbers, the development of the instability is driven by the most energetic one (the first one, $k = 1$, in the present case).[16] Figure 3 shows the temporal evolution of the first two Fourier coefficients $E_k^{1/2}$ and a good agreement with the value predicted by the linear stability theory.[16] In addition, the saturation of the first mode is predicted at approximately $t_j = 40$, corresponding to the region of fully developed turbulence. The spectra of kinetic energy $E(k)$ in Fig. 4 show that the inertial range $-5/3$ slope is well recovered by the simulations for the larger and mid length scales. As expected, the deviation from the inertial range slope takes place at higher

wave numbers for the mesh 2, because of the lower grid dissipation.

The centerline evolutions of the axial velocity and passive scalar concentration are reported in Fig. 5 which shows the rapid decay occurring at $t_j = 30$, corresponding to the beginning of the transitional phase (brackets $< \cdot >_z$ indicate $z-$average). A detailed view of the mean axial velocity radial distribution is shown in the profiles of Fig. 6. They have been obtained by first interpolating w into a polar grid, i.e. $w(x, y, z) \rightarrow w(r, \theta, z)$, and then averaging along the axial, z, and azimuthal, θ directions (represented by brackets, $< \cdot >$). The profiles are scaled by the jet half-width $r_{1/2}$ which is defined as the distance from the center where the axial velocity is half the value at the centerline. The collapse of the curves indicates the emergence of a "self similar period" starting at $t_j = 30$ (as observed by Ghosal and Rogers,[53] although the definition of self-similarity is appropriate in spatially evolving flows where all the variables are time averaged, it is still possible to define a self similar period in temporally evolving flows, where the variables are spatially averaged along the periodic directions).

Transition to turbulence is associated to the formation of structure with high azimuthal vorticity which causes the roll-up of the jet through a Kelvin-Helmotz instability mechanism, as shown in the vorticity iso-contours of Fig. 7. To study the mixing process (Fig. 7) the evolution of a selected passive scalar iso-surface is analyzed at representative times: at the beginning ($t_j = 20$) and middle ($t_j = 30$) instants of the linear stability phase and in the region of fully developed turbulence ($t_j = 42$). At $t_j = 30$, large-scale engulfing of pure fluid from the external air characterizes mixing after the vortex roll-up and before the region of developed turbulence.[54] As observed in DNS of spatially evolving jets,[55] this structure is associated to a switch from marching to non-marching Probability Density Function (PDF) of the passive scalar. According to the definition of Karasso and Mungal,[56] in a marching PDF the most probable state follows the local mean value across a shear layer, while in a non-marching PDF it remains at a constant value irrespective of the local mean value. Figure 8 shows the PDF evolution at selected radial distances from the center. At $t_j = 20$ peak values at each station correspond to mean values, in a clear marching behavior. Later

on, at $t_j = 30$, the two great peaks corresponding to non-mixed fluid are still clearly visible, but, as r decreases, peak values do not follow the mean value, suggesting a non-marching PDF. Finally, at $t_j = 42$, no peak corresponds to pure jet fluid as it is completely mixed with air (the maximum level at the centerline is approximately 0.3, see Fig. 5) and the PDF turns back to a marching behavior dominated by small scale mixing. We thus recover here the same qualitative behavior of DNS of spatial evolving jets,[55] i.e., marching PDF from the nozzle exit to the vortex roll-up and in the region of fully developed turbulence region, and non-marching between the two.

The extension of the mixing zone is reported in Fig. 9, which displays time history of the plume area $A_p(t)$. It is defined as the area where the local mixedness function

$$Z(x,y) = \frac{1}{L_z}\int_0^{L_z} Y(x,y)(1-Y(x,y))dz \tag{17}$$

is greater than a minimum value Z_{min} (here we assumed $Z_{min} = 0.001$, a different choice of such a threshold only causes a global displacement of the curve but does not affect its slope). Results show that A_p remains constant up to the transition ($t_j \simeq 20$) and then increases linearly with a slope $\chi_p = d(A_p/\pi r_j^2)/dt_j \simeq 0.31$. Figure 9 provides the evolution of the total mixedness function Z_V:[57]

$$Z_V = \frac{4}{V}\int_V Y(1-Y)dV \tag{18}$$

where $V = L_x \times L_y \times L_z$ is the volume of the computational domain. Z_V is a measure of the global mixing (0 corresponds to completely unmixed flows, 1 is for fully mixed flows, $Y = 0.5$); the slope of Z_V reduces asymptotically as a consequence of the increasing homogeneity between the passive scalar and the external air. The figure also shows no significant effects of grid resolution on both A_p and Z_V evolutions.

B. Interaction phase

The interaction phase starts when the maximum jet velocity has reduced half its initial value, at $t_j = t_{jv} \simeq 42$ (for example, assuming $r_j = 1.6\,m$ and $w_j = 60\,m/s$, it corresponds

to $t = 1.12\,s$ and a distance from the engine exit of $d = 1.3\,B$, being $B = 60m$ the wing span, a reasonable value for the end of the jet phase). Trailing vortices are usually represented by the Lamb-Oseen model ($\alpha = 1.4$ and $\beta = 1.2544$):

$$v_\theta(r) = \alpha\, v_c \frac{r_c}{r}\left(1 - \exp(-\beta\, r^2/r_c^2)\right) \tag{19}$$

$$\frac{dp}{dr} = \rho \frac{v_\theta^2}{r} \tag{20}$$

which is defined by the core radius and velocity, respectively, r_c and v_c. To study the jet/vortex interaction the computational domain was enlarged in the cross-stream direction with lateral boundaries placed far enough to avoid an interaction with the vortex-induced inflow velocity. The new domain has dimensions $L_x = L_y = 30\,r_j, L_z = 6\,r_j$ and has 301x301x61 nodes (for simplicity $r_c = r_j$) and the initial relative position of the jet with respect to the vortex is given by $x_{jv} = 5\,r_c$, $y_{jv} = -r_c$, as sketched in Fig. 2. The initial jet-to-vortex velocity ratio is $w_j/v_c = 1.5$. Physical time is non-dimensionalized by the vortex characteristic time, i.e. $t_v = t/t_{eddy}$, with $t_{eddy} = 2\pi r_c/v_c$, and its origin is reset to zero.

The dynamics of the interaction is dominated by the entrainment of the jet inside the vortex field. The structure of entrainment process is shown in Fig. 10 which displays the evolution of the iso-surface of the vorticity magnitude corresponding to a level $\omega = \omega_{max}/e^\beta$, ω_{max} being the actual maximum vorticity (the value which identifies the core of an undeformed Lamb-Oseen vortex). The results suggest a process in three stages: in a first stage (see Fig. 10a) the vortex velocity induces the entrainment of the jet around the core which, on the other hand, remains unaffected. Later on, the jet is close enough to the core for its axial velocity to strongly interact with the vortex tangential velocity, causing the emergence of three-dimensional structures of azimuthal vorticity ("rings") around it (Fig. 10b). The formation of this structures can be explained by looking at azimuthal vorticity equation, in its incompressible form:[52]

$$\frac{D\omega_\theta}{Dt} = \omega_r \frac{\partial v_\theta}{\partial r} + \frac{\omega_\theta}{r}\frac{\partial v_\theta}{\partial \theta} + \omega_z \frac{\partial v_\theta}{\partial z} \tag{21}$$

where $D(\cdot)/Dt$ is the total derivative. At the beginning of the entrainment phase radial and tangential vorticity components are zero around the core, $\omega_r = \omega_\theta \simeq 0$. However, as the jet is wrapped around the vortex, it induces axial variation to the velocity field, leading to $\frac{\partial \omega_\theta}{\partial t} \simeq \omega_z \frac{\partial v_\theta}{\partial z} \neq 0$. At the end of the interaction, these azimuthal structures progressively decay and only the vortex core remains as shown in Fig. 10c. Figure 11 displays the maximum value of the azimuthal vorticity, $\omega_{\theta_c}^{peak}$, in a domain of $2r_c$ surrounding the core (to eliminate the contribution of the far jet). In this figure the times corresponding to the three stages are visible. At $t_v = 4$, corresponding to the peak value of ω_θ, Fig. 12 shows the ω_x contour field on a plane passing through the vortex center, superimposed to the axial vorticity iso-contour lines, identifying the core. Transverse vorticity structures of opposite sign (contra-rotative) are observed, causing a mutual interaction which successively leads to their fusion and decay (as often observed in wake vortex dynamics).[31] Besides the formation of azimuthal structures, the jet also induces a global rigid motion of the vortex core as shown in Fig. 10 and in more detail in Fig. 13. Here, the vortex dynamics are tracked as follows: first, the axial vorticity ω_z is computed at each plane along the periodic direction z; then, the two iso-contour lines, corresponding to $\omega_{z_{max}}$ and $\omega_{z_{max}}/e^\beta$, are used to identify, respectively, the center of the vortex and the core radius; finally, these data are averaged along z. Figure 13 shows that, as jet wraps around the core, the moves vertically, reaching two core radii below its original position, at $t_v = 4$. Finally, the mean tangential velocity profiles reported in Fig. 14 show that v_θ is slightly affected by the jet: core velocity does not change up to $t_v \simeq 8$ and a decay of only some percent is observe at the final time, $t_v = 17$. Indeed, as the jet remains outside the core, no strong perturbations are injected in the inner region of the vortex, that may cause its instability. This represents a significant difference with the blowing case that will be analyzed in the next section.

In this phase both turbulent jet dispersion and vortex-induced entrainment control the mixing. As the tangential velocity v_θ varies with the distance from the vortex center, mass elements in the jet experience different entrainment velocities and trajectories (the closer to the core, the faster). A simple mode can be devised to suitably represent the vortex-induced

pure entrainment. The model consists of computing the evolution of a set of 360 Lagrangian points, initially placed along a circumference of radius $r_0 = \sqrt{A_p(0)}/\pi$, where $A_p(0)$ is the plume area at the beginning of the interaction phase. They are initially equi-spaced with $\Delta\phi = 1\,\mathrm{deg}$, and evolve according to the tangential velocity induced by the vortex, $v_\theta(r)$, where r represents the distance from the actual vortex center. The evolution is reported in Fig. 15 and compared with the distribution of the local mixedness field $Z(x, y)$ (see Eqn. (17)). The figure shows a qualitative agreement, with the core remaining unaffected, and different branches forming in the jet structure due to differential entrainment velocity. The results show that mixing process is characterized by a wrapping-like entrainment, driven by v_θ, (in the early stage, $t_v < 4$) plus a jet-like dispersion driven by turbulent diffusion in the last stage. Indeed, after complete wrapping of the jet, the vortex cannot entrain other mass, so that only radial velocity dominates the (small scales) turbulent mixing. The evolution of the plume area A_p reported in Fig. 16 for both the jet and the interaction phases confirms that jet-like dispersion dominates mixing at the end of interaction process, as the plume area asymptotically scales with the same slope as in the jet phase. Although the azimuthal vorticity structures discussed in the previous section may locally alter passive scalar distribution, as shown in Fig. 10b or DNS results,[10] they rapidly decay due to the collision of contra-rotating vortex rings (other effects, not considered here, as the vortex relaminarizing action, can also affect mixing and plume evolution in the far-field). The picture given above is strictly valid outside the vortex core, $r > r_c$. The inner region remains laminar and the solid body-type rotation (see Eqn. (19)) prevents the passive scalar from penetrating inside through radial velocity fluctuations, as shown in the plane cuts of Fig. 10. The reported scalar levels show that the jet experiences high dispersion with the peak value, Y_{max}, decreasing by about 80% of the value at the beginning of the interaction, while the total mixedness Z_V increases to twice the initial value (Fig. 17).

IV. BLOWING CASE

We now analyze another configuration where the jet partially blows inside the vortex core, corresponding to the interaction between the external jet and the flap vortex in a four-engines aircraft, during take-off/landing phases (Fig. 18). It consists of 301x301x61 nodes with $L_x = L_y = 30\, r_c, L_z = 6r_c$, where r_c is the vortex core radius (taken as reference length) while $r_j = 2r_c$ is the jet radius. The origin is taken at the vortex center, the jet and vortex axes are slightly displaced in the vertical direction, $x_{jv} = 0$, $y_{jv} = -2r_c$. Top-hat (Eqn. 14) and Lamb-Oseen (Eqn. 19) profiles are used to initialize the axial, $w(r)$, and tangential, $v_\theta(r)$, velocities, respectively. Passive scalar follows the same *tanh* distribution of Eqn. 16. Time is non-dimensionalized by the eddy time: $t_v = t/t_{eddy}$, where $t_{eddy} = 2\pi r_c/v_c$.
No temporal splitting is adopted because the jet and the vortex are close enough for the interaction to start immediately. Indeed, the jet rapidly wraps around the vortex making this flow similar to a swirling jet or a Batchelor ("q-") vortex.[58] A q-vortex is composed by a Lamb-Oseen vortex and a Gaussian axial flow:

$$v_\theta(r) = \sqrt{\beta}\,\alpha\, v_c \frac{a_c}{r}\left(1 - \exp(-r^2/{a_c}^2)\right) \tag{22}$$

$$w(r) = w_j\, \exp\left(-r^2/{a_c}^2\right) \tag{23}$$

where the dispersion radius $a_c = 1/\sqrt{\beta}\, r_c = 1/1.12\, r_c$ is used instead of core radius r_c. Such a flow is usually studied[25,32] by introducing the swirl parameter q, relating peak axial (w_j) and tangential (v_c) velocities,

$$q = \sqrt{\beta}\,\alpha\, \frac{v_c}{w_j} \simeq 1.57\, \frac{v_c}{w_j} \tag{24}$$

An equivalent definition can be devised, based on circulation $\Gamma(r)$ and integral axial momentum $W(r)$:

$$\Gamma(r) = \int_0^{2\pi}\int_0^r \omega_z(\zeta)\zeta d\zeta d\theta = 2\pi\alpha v_c r_c \left(1 - \exp\left(-r^2/a_c^2\right)\right) \tag{25}$$

$$W(r) = \int_0^{2\pi}\int_0^r w(\zeta)\zeta d\zeta d\theta = 2\pi w_j \frac{a_c^2}{2}\left(1 - \exp\left(-r^2/a_c^2\right)\right) \tag{26}$$

where $\omega_z(r) = \frac{1}{r}\frac{(drv_\theta)}{dr}$ is the axial vorticity. Using Eqns. 24-26 leads to $\Gamma(r)/W(r) = 2q/a_c = const.$ In a q-vortex, the swirl can be deduced from Γ and W at any radial distance r. In particular, in the limit $r \to \infty$, one has:

$$q = \frac{a_c}{2}\frac{\Gamma(r)}{W(r)} = \frac{a_c}{2}\frac{\overline{\Gamma}}{\overline{W}} \tag{27}$$

where $\overline{\Gamma} = \lim_{r\to\infty}\Gamma(r)$ and $\overline{W} = \lim_{r\to\infty}W(r)$ are the total circulation and integral axial momentum, respectively. Equation 27 is well adapted to define the swirl in regions of more complex axial flow, as in the present case, where the jet and the vortex are not exactly concentric and the radii are different. Indeed, it is still meaningful if r is taken sufficiently large to account for most of the circulation and the axial momentum affecting the blowing jet region (in practice we take $r = 2\,r_c$, see Fig. 22b in the following).

Two values of the ratio w_j/v_c have been considered here, $w_j/v_c = 1.5$ (as in the previous section) and $w_j/v_c = 3$. Using Eqn. 27 with $r = 2\,r_c$ gives, respectively, $q \simeq 0.5$ and $q \simeq 0.25$, below the stability limit $q = 1.5$ found by Mayer and Powell.[25] Previous numerical simulations of a Batchelor vortex performed by the same authors[31,39] have shown that q increases in the linear stability region and reaches a value of approximately 1.5, corresponding to the saturation of the instability (see Fig. 19a); indeed, the tangential velocity does not vary, while axial momentum decreases, and a relaminarization of the flow is reached at later times.[31,32] As discussed by Jacquin and Pantano,[59] this is related to the existence of a "dispersion buffer", adjacent to the core of a Batchelor vortex. The presence of this buffer zone, whose extent depends on the initial q, prevents perturbations or turbulence generated inside the core from being amplified when reaching the vortex periphery. For high initial swirl, this results in a continuous damping of axial flow, leading to an increases of q and the stability of the flow. However, for low swirl, it is argued[59] that turbulence may succeed in breaking the stability by transporting angular momentum outside the core, as in in the experiments of Phillips and Graham[60] (case A, where $q \simeq 0.4$), as well as in the present blowing jet simulations. Indeed, for both values $w_j/v_c = 1.5$ and 3, Fig. 19b shows only a slight increase of q up to $t_v = 1$, followed by a rapid decay. This is coherent with the

evolution of the tangential velocity profiles shown in Fig. 20. After $t_v = 1$, the interaction with the unstable blowing jet causes a strong deformation of the velocity profiles, by increasing vortex core size and reducing peak velocity (up to 1/2 v_c at $t_v = 4$). Moreover, the radial distribution of circulation $\Gamma(r)$ in Fig. 21 shows the propagation of a high overshoot, which indicates diffusion of angular momentum outside the core, as also observed by Jacquin and Pantano.[59] This behavior can be explained by looking at the flow structure in Fig. 22 which shows a two-dimensional contour field of axial flow w, superimposed to the vorticity iso-surface $\omega = \omega_{max}/e^{\beta}$. During the instability process that leads to the transition to turbulence, the jet partly wraps around the vortex and partly penetrates into its core where it injects strong axial perturbations (swirl is low). Such a process is continuously fed by the (still energetic) axial flow present in the periphery of the vortex, which has indeed the role of an energy reservoir for the whole instability mechanism (as also shown by the evolution of axial velocity profiles in Fig. 20b). This instability, combined with the low swirl, is responsible for the strong decay of angular momentum, diffusion of the core and deformation of the vortex structure. Indeed, the iso-surface of the λ_2 invariant[61] of Fig. 23 shows that, for the case $w_j/v_c = 3$, at $t_v = 4$, the large-scale vortex coherence is lost, whereas the total circulation remains constant far from the core. Note the difference with a Batchelor vortex where all axial flow is concentrated in the core, axial momentum rapidly decays, leaving the vortex core almost unaffected.[31,32]

We conclude this section looking at global mixing. Figure 24 shows the time history of global mixedness Z_V (calculated as in Sec. III): both the level and the rate of variation of Z_V increase with the jet strength, suggesting faster global mixing for the case $w_j/v_c = 3$. This is in agreement with the evolutions of plume areas A_p reported in Fig. 25, showing the results for the jet entrainment case too (both the jet phase and the beginning of the interaction phase, see Sec. III). For the two blowing jet cases, plume areas scale linearly with rates, $\chi_p = d(A_p/\pi\, r_j^2)/dt_v \simeq 1.4$ and 4.6, respectively. In addition, the jet remains concentrated (smaller plume areas) because of the absence of large scale vortex entrainment (it immediately wraps around the vortex, as discussed above).

V. APPLICATIONS TO ENVIRONMENTAL PROBLEMS

The present LES results can be analyzed in terms of environmental problems. The first issue is the modification of the emission index[4] of an exhaust species due to plume dispersion in the atmosphere. This is important to evaluate global emissions used in climate codes. The second one is the prediction of contrails formation due to water vapor condensation. These two problems can be treated in a first approach in the same way, by applying post-processing models to jet/vortex simulations.

1. Reduction of the emission index

The impact of aircraft emissions on the environment depends on the mixing properties between exhaust gases and air. A suitable measure of mixing is the mixture fraction,

$$\zeta = \frac{Y_k - Y_k^a}{Y_k^j - Y_k^a} \tag{28}$$

where Y_k is a generic transported (inert) species. Using Eqn. 16, the initial ζ profile is easily found to be:

$$\zeta_0(r) = \frac{1}{2}\left\{1 - \tanh\left[\frac{1}{4}\frac{r_j}{\theta}\left(\frac{r}{r_j} - \frac{r_j}{r}\right)\right]\right\} \tag{29}$$

Without loss of generality, the atmosphere is assumed to be free of the species emitted by the engine, $Y_k^a = 0$, so that $Y_k = \zeta\, Y_k^j$. The analysis given in the previous section allows to define equivalent parameters of the engine (as, for example, the emission index, EI) which accurately take into account plume dispersion. For a given species k, the emission index is defined as $EI_k = m_k/m_f$ where m_k is the total mass of species k emitted by the engine and m_f is the mass of fuel. By introducing the dilution ratio, $N(t) = m_p(t)/m_f$ (see, for instance Schumann *et al*),[5] where $m_p(t)$ is the actual mass of the plume, one can form the "equivalent" emission index EI_k^{eq} as

$$EI_k^{eq}(t) = \frac{EI_k}{N(t)} = \frac{m_k}{m_p(t)} = \frac{\displaystyle\int_{A_p(0)} \rho Y_k\, dA}{\displaystyle\int_{A_p(t)} \rho\, dA} = \frac{Y_k^j \displaystyle\int_{A_p(0)} \rho\,\zeta\, dA}{\displaystyle\int_{A_p(t)} \rho\, dA} = Y_k^j\, \frac{m_\zeta}{m_p(t)} \tag{30}$$

Equation (30) shows that the evolution of EI_k^{eq} is controlled by the initial concentration of the species Y_k^j and by the total mass of the plume $m_p(t)$, as confirmed in Fig. 26 which shows the time histories of EI_k^{eq} for typical emitted species.[7] The evolutions are compared for the entrainment and the blowing jet cases. The figure shows that dilution causes a strong reduction of EI_k^{eq}. However, in the entrainment case, such a reduction mainly takes place during the transitional jet phase and the beginning of the interaction phase (up to $t_v \simeq 6$), before the jet completely wraps around the vortex; in the blowing jet cases, EI_k^{eq} is initially lower because the rapid interaction with the vortex causes a faster instability of the jet and higher mixing and dilution rates.

2. Contrail formation

Contrails are ice clouds generated by hot exhaust vapor condensation, during mixing with cold ambient air. They form when the water vapor partial pressure, $p_w = p\,X_w$ (X_w is the vapor molar fraction, $Y_w = W_w/\overline{W}\,X_w = 0.621\,X_w$) locally exceed the theoretical ice saturation limit, $p_{sat}(T)$, given by:[62]

$$\ln p_{sat}(T) = -\frac{6024.5282}{T} + 29.32707 + 1.0613868\,10^{-2}\,T \tag{31}$$

$$-1.3198825\,10^{-5}\,T^2 - 0.49382577\,\ln T \tag{32}$$

If this is the case and, at the same time, suitable nucleation sites like soot or aerosols are present, ice starts to depose on the surface of the sites and a condensation trail ("contrail") forms.[4] In the present simulations, it is possible to check the conditions of contrail formation by following the evolution of the thermodynamic state (T, p_w) of the jet. To that end, a last set of simulations was carried out (for the jet phase of Sec. III), assuming a temperature gradient at the initial jet interface, $S_T = T_j/T_a = 2$ (typical values of ambient air and real exhaust gases are $210K < T_a < 270K$ and $T_j < 600K$). The initial condition follows the same law Eqn. 16 for a passive scalar:

$$T_0(r) = \frac{1}{2}\left\{(T_j + T_a) - (T_j - T_a)\tanh\left[\frac{1}{4}\frac{1}{\theta}\left(r - \frac{1}{r}\right)\right]\right\} \tag{33}$$

Assuming the same (ambient) pressure, the corresponding density ratio is $S_\rho = \rho_j/\rho_a = 0.5$, below the limit of absolute instability ($S_\rho = 0.72$) found by Monkewitz and Sohn.[22] As the Mach number is low, dilatation is small and kinetic energy is negligible compared to static enthalpy. Therefore, temperature and water partial pressure can be treated as passive scalars, evolving along the following mixing line (obtained by elimination of r from Eqns. (29) and (33)):

$$\frac{p_w}{p_w^j - p_w^a} = \frac{T}{T_j - T_a} + \frac{1}{2}\left(\frac{p_w^j + p_w^a}{p_w^j - p_w^a} - \frac{T_j + T_a}{T_j - T_a}\right) \tag{34}$$

which is obtained by eliminating r from Eqns. (33) and (29). To show the influence of the initial water vapor emissions X_w^j on the contrail formation, Fig. 27 displays three different scatter plots of p_w versus T (corresponding to three different p_w^j, i.e. three mixing lines) superimposed to the saturation curve Eqn. (32). For given atmospheric conditions, the slope of the mixing line controls contrails formation: as expected, an engine emitting less water vapor will lead to condensation at lower ambient temperatures and eventually will not cause condensation (case $X_w^j = 0.01$).

VI. CONCLUSIONS

This paper reports LES of the interaction between an exhaust jet and a trailing vortex, in the near-field of an aircraft wake. We analyzed two different configurations, representative, respectively, of cruise flight and high lift flight of four-engines aircrafts.

In the first case, the jet and the vortex are initially well separated which allows a two-step simulation. It consists in first simulating the jet evolution and then its interaction with the wake vortex. The dynamics and mixing of the interaction are mainly controlled by entrainment of the jet by the vortex and the turbulent diffusion of the jet. Other phenomena were identified, like the formation of vortex rings and a global rigid motion of the whole system. Two mechanisms were found to control mixing, i.e. wrapping-like entrainment of exhaust gases and turbulent diffusion of the jet. Finally, the solid-body rotation of the

core prevents passive scalar from penetrating inside the vortex. In the second case, the jet partially blows inside the vortex field, making this flow similar to a Batchelor vortex. An instability mechanism was identified, which is due to the strong injection of axial flow perturbations in the core and the continuous feed by the jet elements, wrapping around the core itself. This leads to a strong decay of angular momentum and diffusion of the vortex core. Due to the absence of large-scale vortex entrainment, plume area remains more concentrated with respect to the first case analyzed. This has an impact on the dilution of exhaust species in the atmosphere, for which two environmental applications are finally presented.

REFERENCES

[1] P.R. Spalart Airplane trailing vortices *Ann. Rev. Fluid. Mech.*, vol. 30, 1998.

[2] V.J. Rossow. Lift-generated vortex wakes of subsonic transport aircraft. *Prog. Aer. Sc.*, 35, 507-660, 1999.

[3] Aviation and global atmosphere. Special Report of the Intergovernmental Panel on Climate Change (IPCC). 1999 Cambridge University Press.

[4] U. Schumann. On the conditions for contrails formation. *Meteorol. Zeitschrift*, 5, 4-23, 1996.

[5] U. Schumann., H. Schlager, F. Arnold, R. Baumann, P. Haschberger and O. Klemm. Diluition of aircraft exhaust plumes at cruise altitudes. *Atm. Environ.*, 32, 3097-3103, 1998.

[6] P. Schulte, H. Schlager, H. Ziereis, U. Schumann, S.L. Baughcum and F. Deidewig. NO_x emission indeces of subsonic long-range jet aircraft at cruise altitude: In situ measurements and predictons. *J. Geophys. Res., 102*, 21,431-21,442, 1997.

[7] F. Garnier, C. Baudoin, P. Woods and N. Louisnard. Engine emission alteration in the near-field of an aircraft. *Atm. Environ.*, 31, 1767-1781, 1997.

[8] T. Gerz, T. Durbeck and P. Konopka, Transport and effective diffusion of aircraft emissions. *J. Geophys. Res., 103*, 25,905-25,913, 1998.

[9] R.C. Myake-Lye, R.C. Brown, C.E. Kolb. Plume and wake dynamics, mixing and chemistry behind a high speed civil transport aircraft. *J. Aircraft*, 30, 467-479, 1993.

[10] C. Ferreira Gago, S. Brunet and F. Garnier. Numerical Investigation of turbulent mixing in a jet/wake vortex interaction. *AIAA J.*, 40, 276-284, 2002.

[11] L. Jacquin and F. Garnier. On the dynamics of Engine Jets behind a Transport Aircraft. *AGARD-CP-584* 37, 1996.

[12] T. Gerz and T. Ehret. Wake dynamics and exhaust distribution behind cruising aircraft. *AGARD-CP-584* 35, 1996.

[13] S. Brunet , F. Garnier and L. Jacquin. Numerical/experimental simulation of exhaust jet mixing in wake vortex. *AIAA paper no. 99-3418*, 1999.

[14] E. Fares, M. Meinke and W. Schroeder. Numerical simulation of the interaction of wingtip vortices and engine jets in the near field. *AIAA paper no. 2000-2222*, 2000.

[15] A. Michalke and G. Hermann. On the inviscid instability of a circular jet with external flow. *J. Fluid Mech.*, 114, 343-359, 1982.

[16] P. Brancher, 'Etude numérique des instabilités secondaires de jets', PhD thesis, Ecole Polytechnique, 1996, France.

[17] T. Loiseleux, J.M. Chomaz, P. Huerre. The effects of swirl on jets and wakes: Linear instability of the Rankine-vortex with axial vortex. *Phys. Fluids*, 10, 1120-1134, 1998.

[18] G. Lu and S.K. Lele. Inviscid instability of compressible swirling mixing layers. *Phys. Fluids*, 11, 450-461, 1999.

[19] J.B. Freund, S.K. Lele and P. Moin. Numerical simulation of a Mach 1.92 turbulent jet and its sound field. *AIAA J.*, 38, 2023-2031, 2000.

[20] F.P. Ricou and D.B. Spalding. Measurements of entrainment by axisymmetrical turbulent jets. *J. Fluid Mech.*, 11, 21-32, 1961.

[21] G.N. Abramovich, O.V. Yakovleski, I.P. Smirnova, A.N. Secundov and S. Yu. An investigation of the turbulent jets of different gases in a general stream. *Acta Astronautica*, 14, 229, 1969.

[22] P.A. Monkewitz and X.D. Sohn. Absolute instability in hot jets. *AIAA J.*, 26, 911-916, 1988.

[23] P.A. Monkewitz, D.W. Bechert, B. Barsikov and B. Lehmann. Self-excited oscillations and

mixing in a heated round jet. *J. Fluid Mech.*, 213, 611-639, 1990.

[24] P.A. Monkewitz, B. Lehmann, B. Barsikov and D.W. Bechert. The spreading of self-excited hot jets by side jets. *Phys. Fluids A*, 1, 446-448, 1989.

[25] E.W. Mayer and K.G. Powell. Viscous and inviscid instabilities of a trailing vortex. *J. Fluid Mech.*, 245, 91-114, 1992.

[26] G. Hu, D. Sun and X. Yin. A numerical study of dynamics of a temporally evolving swirling jet. *Phys. Fluids*, 13, 951-965, 2001.

[27] W.J. Devenport, M.C. Rife, S.I. Liapis and G. J Follin. The structure and development of a wing-tip vortex. *J. Fluid Mech.*, 312, 67-106, 1996.

[28] W.J. Devenport, J.S. Zsoldos and C.M. Vogel. The structure and development of a counter-rotating wing-tip vortex pair. *J. Fluid Mech.*, 332, 71-104, 1997.

[29] A. Chen, J.D. Jacob and O. Savas. Dynamics of corotating vortex pairs in the wakes of flapped airfoils. *J. Fluid Mech.*, 382, 155-193, 1999.

[30] L. Jacquin, D. Fabre, P. Geffroy and E. Coustols. The properties of a Transport Aircraft Wake in the Extended Near field: An experimental Study. *AIAA Paper no. 2001-1038*, 2001.

[31] F. Laporte. Application of the numerical simulation to the characterization and the instabilities of transport aircraft wake vortices. PhD thesis, Institut National Polytechnique de Toulouse, CERFACS, France.

[32] S. Ragab and M. Sreedhar. Numerical simulation of vortices with axial velocity deficits. *Phys. Fluids*, 7, 549-558, 1995.

[33] J.D. Crouch. Instability and transient growth for two trailing-vortex pairs. *J. Fluid Mech.*, 350, 311-330, 1997.

[34] S.C. Rennich and S.K. Lele. Method for accelerating the destruction of aircraft wake

vortices. *J. Aircraft*, 36, 398-404, 1999.

[35] D. Fabre and L. Jacquin. Stability of a four-vortex aircraft wake model. *Phys. Fluids*, 12, 2438-2443, 2000.

[36] T. Leweke, P. Meunier, F. Laporte and D. Darracq. Controlled interaction of co-rotating vortices. *Proc. 3rd ONERA-DLR Aerospace Symposium, ODAS, Paris*, 2001.

[37] D. Fabre, L. Jacquin and A. Loof. Optimal perturbations in a four-vortex aircraft wake in counter-rotating configuration. *J. Fluid Mech.*, 451, 319-328, 2002.

[38] S. Le Dizès and F. Laporte. Theoretical predictions for the Elliptic instability in a two-vortex flow. *J. Fluid. Mech.*. 471, 169-201, 2002.

[39] R. Paoli, B. Cuenot and F. Laporte. Jet vortex interactions in airplane wakes. *Proc. of the Euromech Colloquium no. 433, Aachen, Germany*, 2002.

[40] M. Gaster. A note on the relation between temporally-increasing and spatially-increasing disturbances in hydrodynamic stability. *J. Fluid Mech.*, 14, 222-224, 1962.

[41] R.L. Le Boeuf and R.D. Metha. On using Taylor's hypothesis for three-dimensional mixing layers. *Phys. Fluids*, 7, 1516-1518, 1995.

[42] G. Erlebacher, M.Y. Hussaini, C.G. Speziale and T. A. Zang. Towards the Large-Eddy Simulation of Compressible Turbulence. *J. Fluid Mech*, 238, 155-185, 1992.

[43] O. Métais and M. Lesieur. Spectral Large-Eddy Simulation of Isotropic and Stably Stratified Turbulence. *J. Fluid. Mech.*, 239, 157-194, 1992.

[44] F. Ducros, P. Comte and M. Lesieur. Large Eddy Simulation of transition to turbulence in a boundary layer spatially developing over a flat plate. *J. Fluid. Mech.*, 326, 1-36, 1996.

[45] F. Laporte and A. Corjon. Direct Numerical Simulations of the elliptic instability of a vortex pair. *Phys. Fluids*, 12, 1016-1031, 2000.

[46] A. Stoessel. An efficient tool for the study of 3D turbulent combustion phenomena on MPP computers. *Proc. of the HPCN 95 Conference, Milan (Italy)*, 306-311, 1995.

[47] L. Gamet, F. Ducros, F. Nicoud and T. Poinsot. Compact finite difference schemes on non-uniform meshes. Application to direct numerical simulations of compressible flows. *Int. J. for Num. Meth. in Fluids*, 39, 159-191, 1999.

[48] S. Chester, F. Charlette and C. Meneveau. Dynamic Model for LES without test-filtering: quantifying the accuracy of Taylor series approximations. *Theoret. Comput. Fluid Dynamics*, 15, 165-181, 2001.

[49] S.K. Lele. Compact finite difference scheme with spectral-like resolution. *J. Comp. Phys.*, 103, 16-42, 1992.

[50] T.J. Poinsot and S.K. Lele. Boundary Conditions for Direct Simulations of Compressible Viscous Flows. *J. Comp. Phys.*, 101, 104-129, 1992.

[51] R. Verzicco and P. Orlandi. Direct simulations of the transitional regime of a circular jet. *Phys. Fluids*, 6, 751-759, 1993.

[52] P.G. Saffman. Vortex Dynamics, Cambridge University Press, 1992.

[53] S. Ghosal and M. Rogers. A numerical study of self-similarity in a turbulent plane wake using large eddy simulations. *Phys. Fluids*, 9, 1729-1739, 1997.

[54] C. Le Ribault, S. Sarkar and S.A. Stanley. Large Eddy Simulations of Evolution of a Passive Scalar in Plane Jet. *AIAA J.*, 39, 1509-1516, 2001.

[55] S.A. Stanley, S. Sarkar and J.P. Mellado. A study of the flow-field evolution and mixing in a planar turbulent jet using direct numerical simulations. *J. Fluid Mech.*, 450, 377-407, 2002.

[56] P.S. Karasso and M.G. Mungal. Scalar Mixing and Recation in Plane Liquid Shear Layers. *J. Fluid Mech.*, 323, 23-63, 1996.

[57] B.M Cetegen and N. Mohamad. Experiments on liquid mixing and reaction in a vortex. *J. Fluid Mech.*, 249, 391-414, 1993.

[58] G. Batchelor. Axial flow in trailing line vortices. *J. Fluid Mech.*, 20, 645-658, 1964.

[59] L. Jacquin and C. Pantano. On the persisitence of trailing vortices. *J. Fluid Mech.*, 471, 159-168, 2002.

[60] W.R.C. Phillips and J.A.H. Graham. Reynolds stress measurements in a turbulent trailing vortex. *J. Fluid Mech.*, 147, 353-371, 1984.

[61] J. Jeong and F. Hussain. On the identification of a vortex. *J. Fluid Mech.*, 285, 69-9, 1995.

[62] D. Sonntag. Advancements in the field of hygrometry. *Meteorol. Zeitschrift*, 3, 51-66, 1994.

FIG. 1. Basic configuration of a jet/vortex interaction in the near-field of an aircraft wake.

FIG. 2. Computational domain for the entrainment case (jet and interaction phases).

FIG. 3. Evolutions of the first two computed Fourier coefficients: ——, $\sqrt{E}_1$; - - -, $\sqrt{E}_2$. The theoretical growth rate of the first mode (Ref. 16) is also represented, $\sigma_1^{th} = 0.026\, w_j/\theta$.

FIG. 4. Kinetic energy spectra E_k at $t_j = 42$: —□— , mesh 1 ($\Delta_x = \Delta_y = \Delta_z = 0.1 r_j$); —○— , mesh 2 ($\Delta_x = \Delta_y = 0.075 r_j, \Delta_z = 0.1 r_j$).

FIG. 5. Centerline evolutions of the $z-$averaged axial velocity $< w_0 >_z$ (——), and passive scalar concentration $< Y_0 >_z$ (- - -).

FIG. 6. Evolutions of non-dimensional half-width-scaled velocity profiles $< w(r) >$, during the "self-similar period" (brackets indicate average in the axial and azimuthal directions).

FIG. 7. Dynamics and mixing during the jet phase: a) $t_j = 20$; b) $t_j = 30$; c) $t_j = 42$. Left side: evolution of transverse vorticity ω_x contour lines, in the $y - z$ plane through the jet centerline (32 levels, solid/dashed lines indicate positive/negative vorticity: a) $\omega_x \in [-2.4; 2.4]$; b) $\omega_x \in [-5.5; 5.5]$; c) $\omega_x \in [-6.0; 6.0]$). Right side: evolution of a selected passive scalar iso-surface, $Y = 0.4$.

FIG. 8. Passive scalar PDF at different distances from the center and different times during the jet phase: a) $t_j = 20$; b) $t_j = 30$; c) $t_j = 42$. Lines-hollow symbols represent the PDF distributions at given radial position r; full symbols on the top represent the corresponding average values.

FIG. 9. Time evolution of the normalized plume area, $A_p/\pi r_j^2$, and mixing function, $Z_V/Z_V(0)$, during the jet phase (——, mesh 1; - - -, mesh 2).

FIG. 10. Evolution of the vorticity magnitude, ω, and passive scalar, Y, during the interaction phase: a) $t_v = 2$; b) $t_v = 4$; c) $t_v = 17$. Left: evolution of a selected iso-surface, $\omega = \omega_{max}/e^{\beta}$, and, superimposed, plane cuts ($z = 0$) of passive scalar iso-contour lines. Right: detailed view of passive scalar field at $z = 0$.

FIG. 11. Time history of the maximum azimuthal vorticity, $\omega_{\theta_c}^{peak}$, around the core, during the jet/vortex interaction phase.

FIG. 12. Azimuthal vorticity contour lines (15 levels, $\omega_x \in [-3.0; 3.0]$) in a transversal plane yz passing through the vortex center ($t_v = 4$, corresponding to the maximum of $\omega_{\theta_c}^{peak}$); the axial vorticity contour field (5 levels, between 0 and $\omega_{z_{max}}$) is superimposed.

FIG. 13. Time history of the location of the vortex core identified by $\omega_{z_{max}}$, vortex center, and $\omega_{z_{max}}/e^{\beta}$, core radius.

FIG. 14. Evolution of $z-$averaged tangential velocity profiles (taken along a line passing through the vortex center): ——, $t_v = 0$, —□— , $t_v = 1$; —○— , $t_v = 4$; —△— , $t_v = 8$; —▽— , $t_v = 17$.

FIG. 15. Evolution of local mixedeness, $Z(x, y)$, contour field and lagrangian body lines, during the interaction phase.

FIG. 16. Time history of the normalized plume area, $A_p/\pi r_j^2$, during the jet and the interaction phases.

FIG. 17. Time histories of peak passive scalar, Y_{max}, and global mixedness, Z_V.

FIG. 18. Computational domain for the blowing jet.

FIG. 19. Time history of the swirl parameter q; a), q-vortex[31]; b) present blowing jet (——, $w_j/v_c = 1.5$; - - -, $w_j/v_c = 3$).

FIG. 20. Evolutions of $z-$averaged tangential (a) and axial (b) velocity profiles (taken along a line passing through the vortex center): ——, $t_v = 0$, —□— , $t_v = 1$; —○— , $t_v = 3$; —△— , $t_v = 4$.

FIG. 21. Evolution of radial distribution of circulation $\Gamma(r)$ for the case $w_j/v_c = 1.5$ (a) and $w_j/v_c = 3$ (b); —□— , $t_v = 1$; —○— , $t_v = 3$; —△— , $t_v = 4$.

FIG. 22. Flow structure at $t_v = 1$: (a) iso-surface of the vorticity magnitude ($\omega = \omega_{max}/e^{\beta}$) and passive scalar plane cut (5 levels from 0 to 1); (b) two-dimensional $z-$averaged contour field of axial velocity (the blowing jet region, $-2r_c < r < 2r_c$, is identified by dashed lines).

FIG. 23. Flow structure at $t_v = 4$ ($w_j/v_c = 3$): (a) iso-surface of λ_2 invariant;[61] (b) two-dimensional $z-$averaged passive scalar contour field.

FIG. 24. Time histories of global mixedness Z_V: ——, $w_j/v_c = 1.5$; - - -, $w_j/v_c = 3$.

FIG. 25. Temporal evolutions of plume areas $A_p/\pi r_j^2$: ——, $w_j/v_c = 1.5$; - - -, $w_j/v_c = 3$; -----, entrainment case (Sec. III).

FIG. 26. Temporal evolutions of the equivalent emission indeces EI^{eq}: for two typical exhaust species (CO_2, —□— ; NO_2, —○—) and different configurations: -----, entrainment case; ——, blowing cae, $w_j/v_c = 1.5$; - - -, blowing case, $w_j/v_c = 3$ (exit mass concentrations taken from literature data:[7] $Y^j_{CO_2} = 4.8\,10^{-2}$, $Y^j_{NO_2} = 1.05\,10^{-4}$).

FIG. 27. Scatter plots of water vapor partial pressure, p_w, and temperature, T, during the jet phase (+, $t_j = 20$; ×, $t_j = 30$; ∗, $t_j = 40$) and for different exit concentrations, $X^j_w = 0.04$, 0.025 and 0.01 (superimposed, the theoretical saturation curve, p_{sat}).

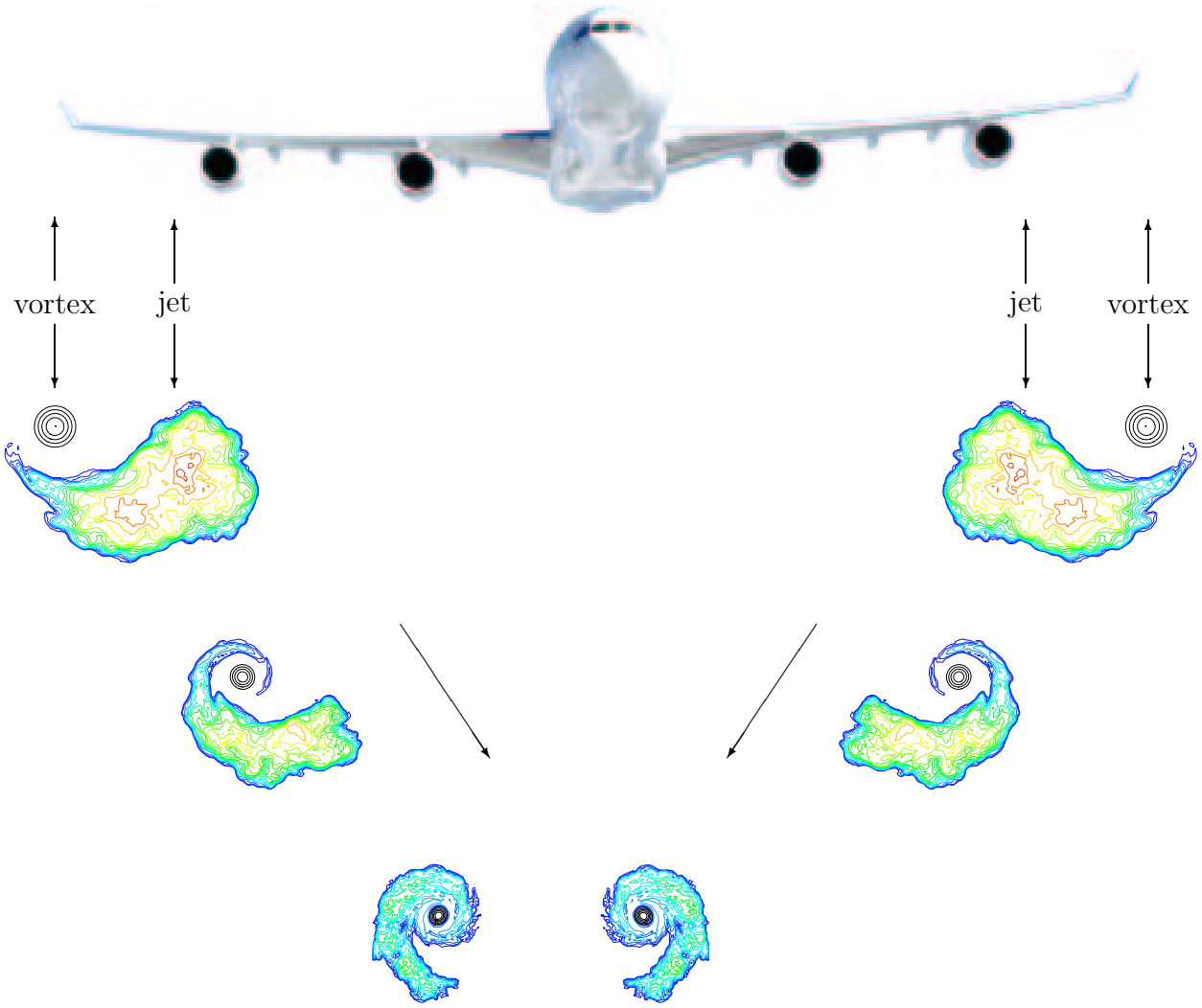

PHYS. FLUIDS – figure 1

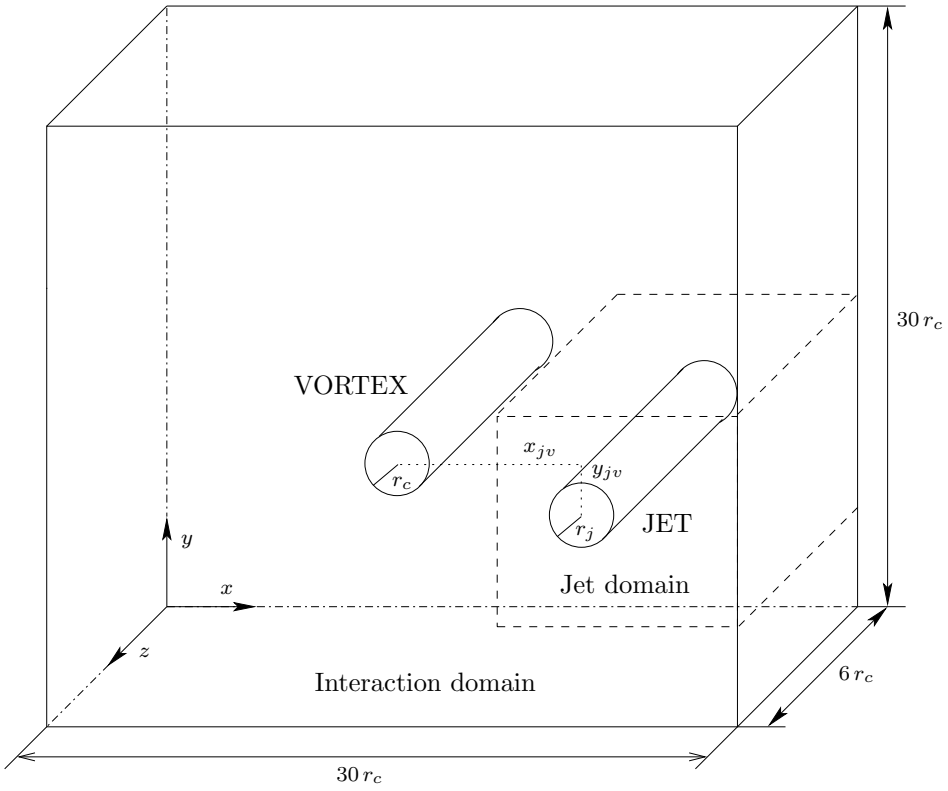

PHYS. FLUIDS – figure 2

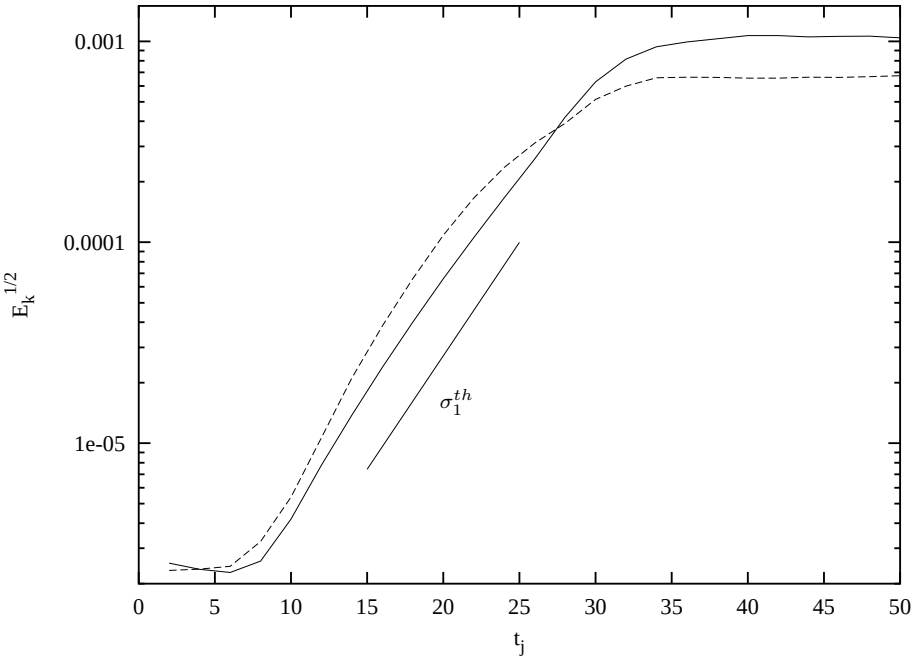

PHYS. FLUIDS – figure 3

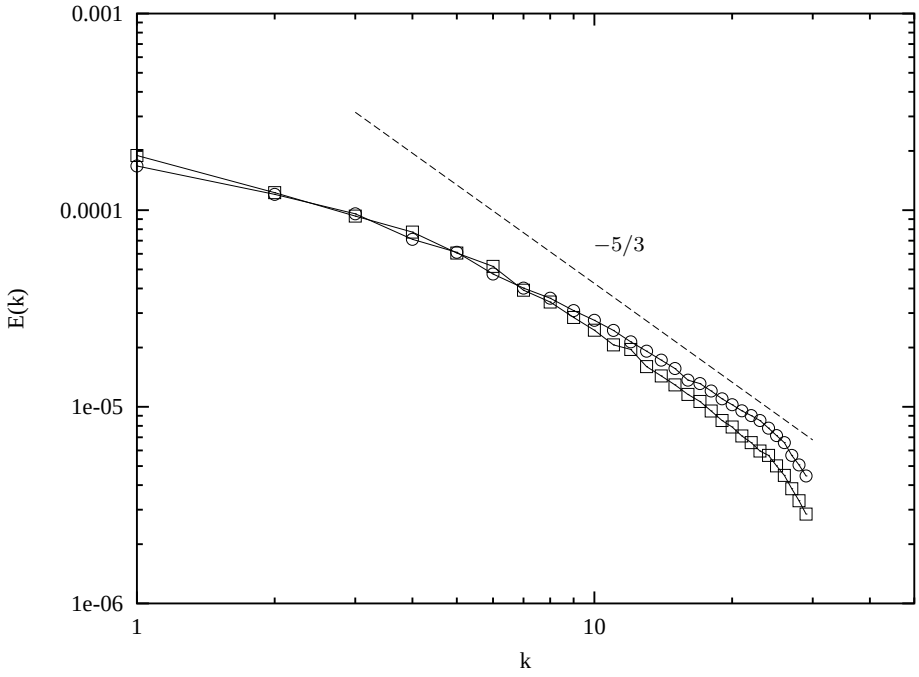

PHYS. FLUIDS – figure 4

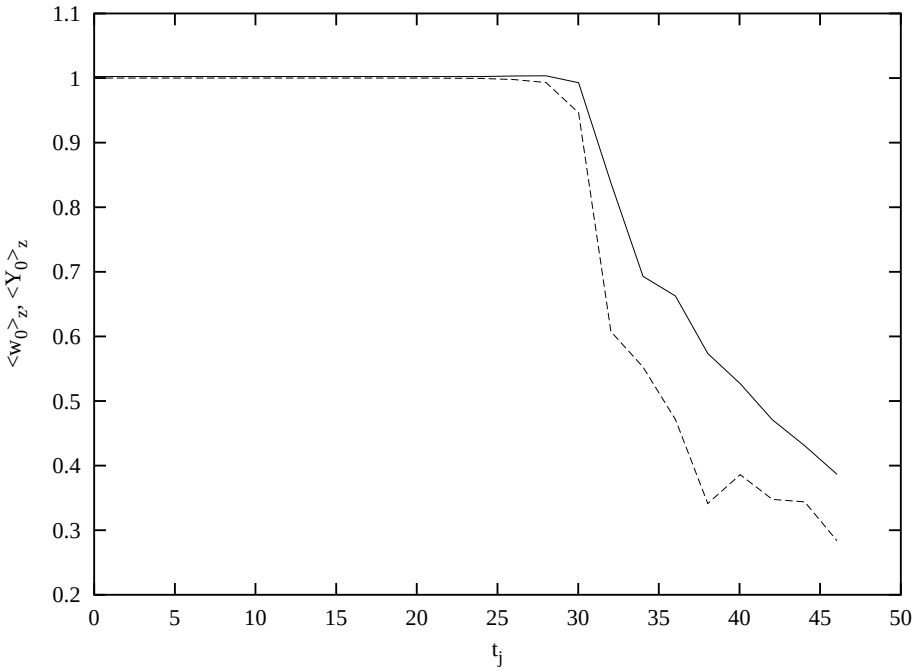

PHYS. FLUIDS – figure 5

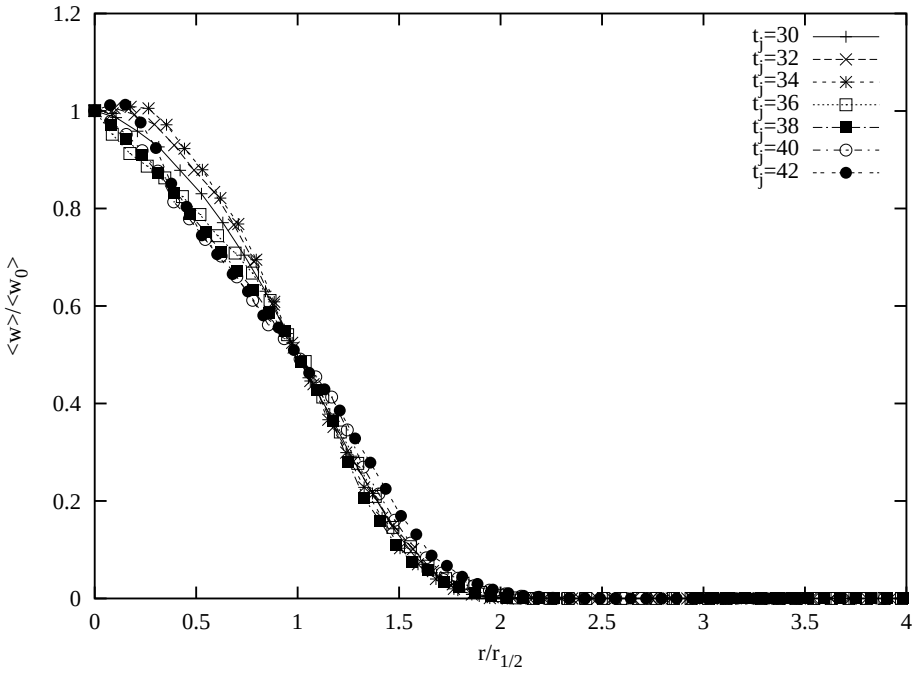

PHYS. FLUIDS – figure 6

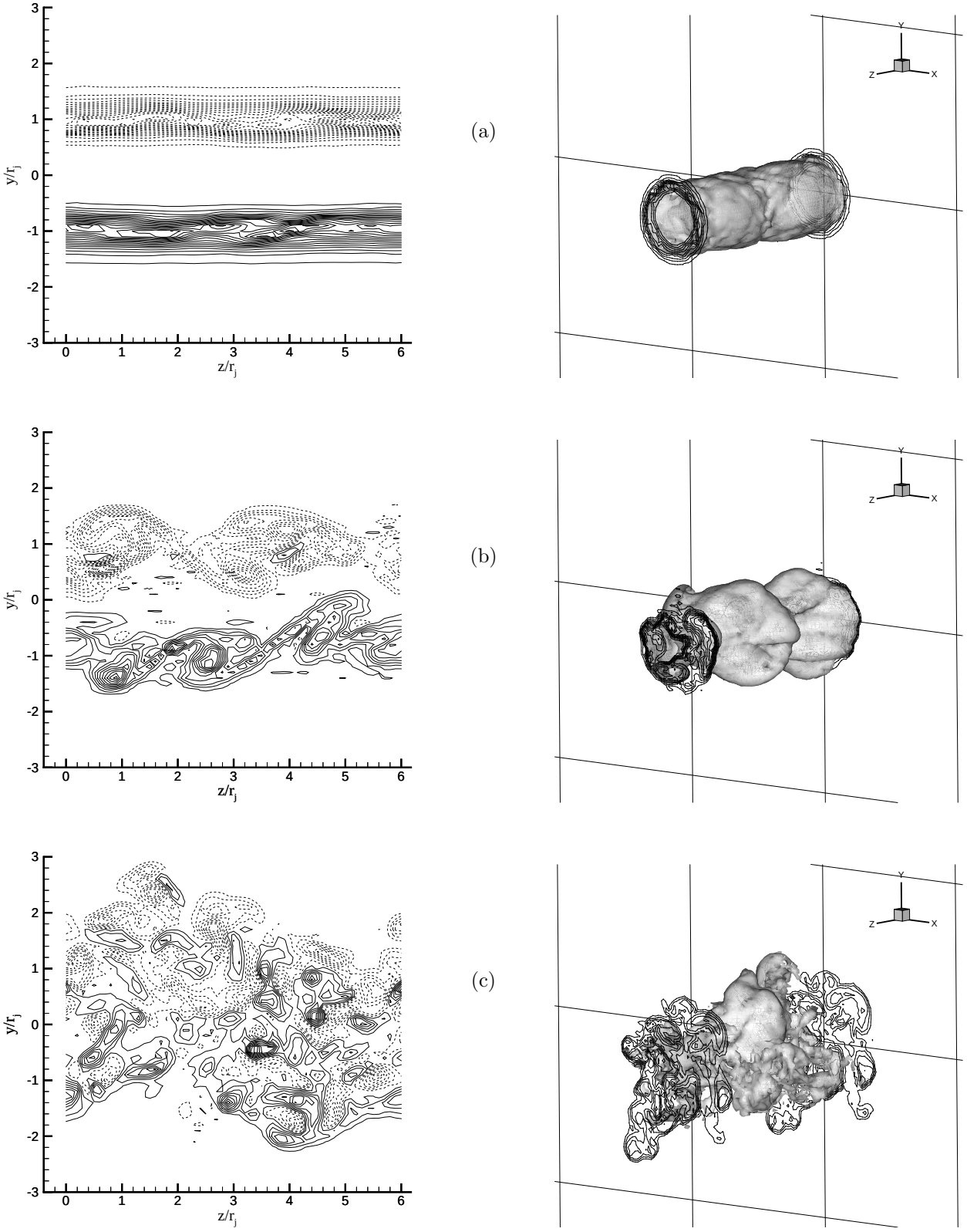

PHYS. FLUIDS – figure 7

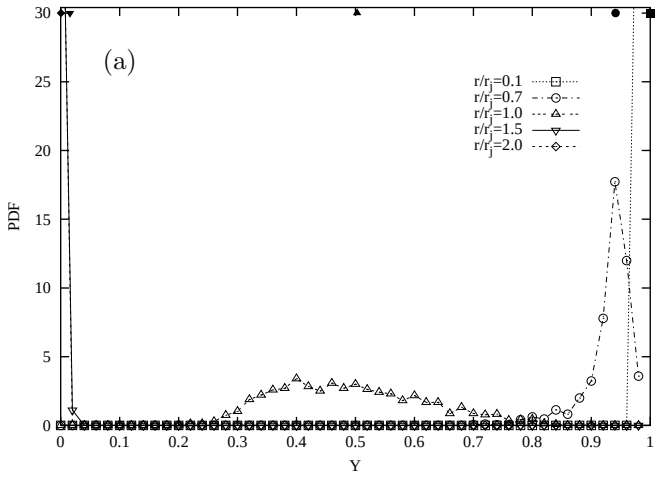

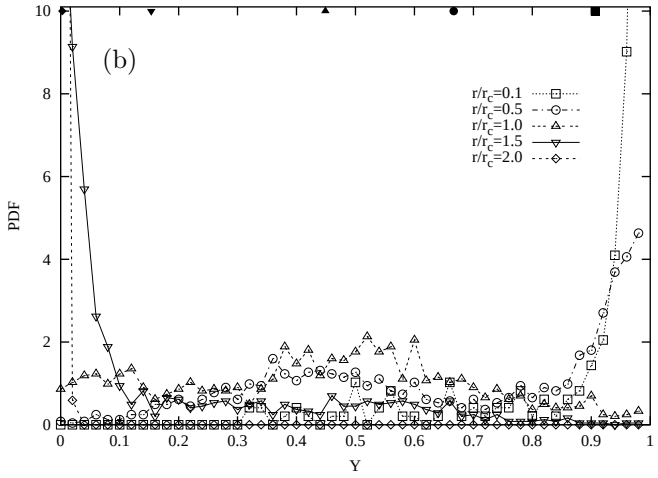

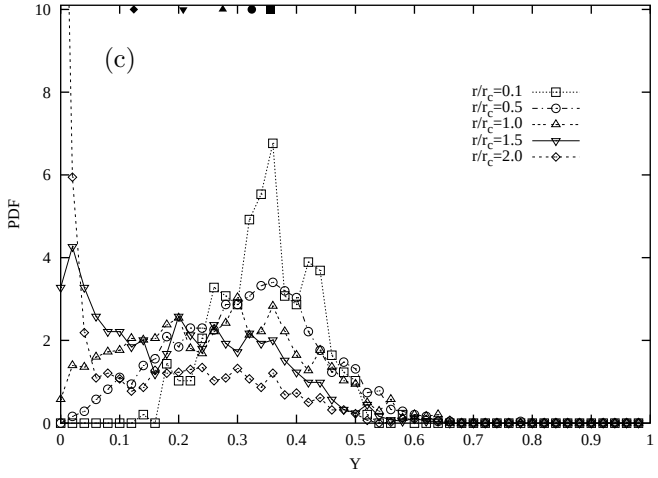

PHYS. FLUIDS – figure 8

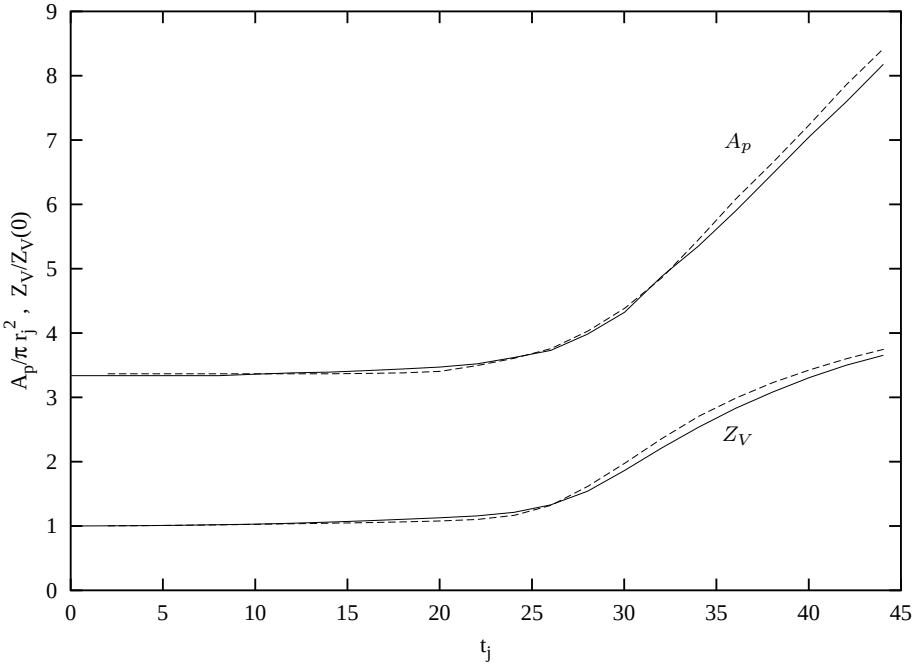

PHYS. FLUIDS – figure 9

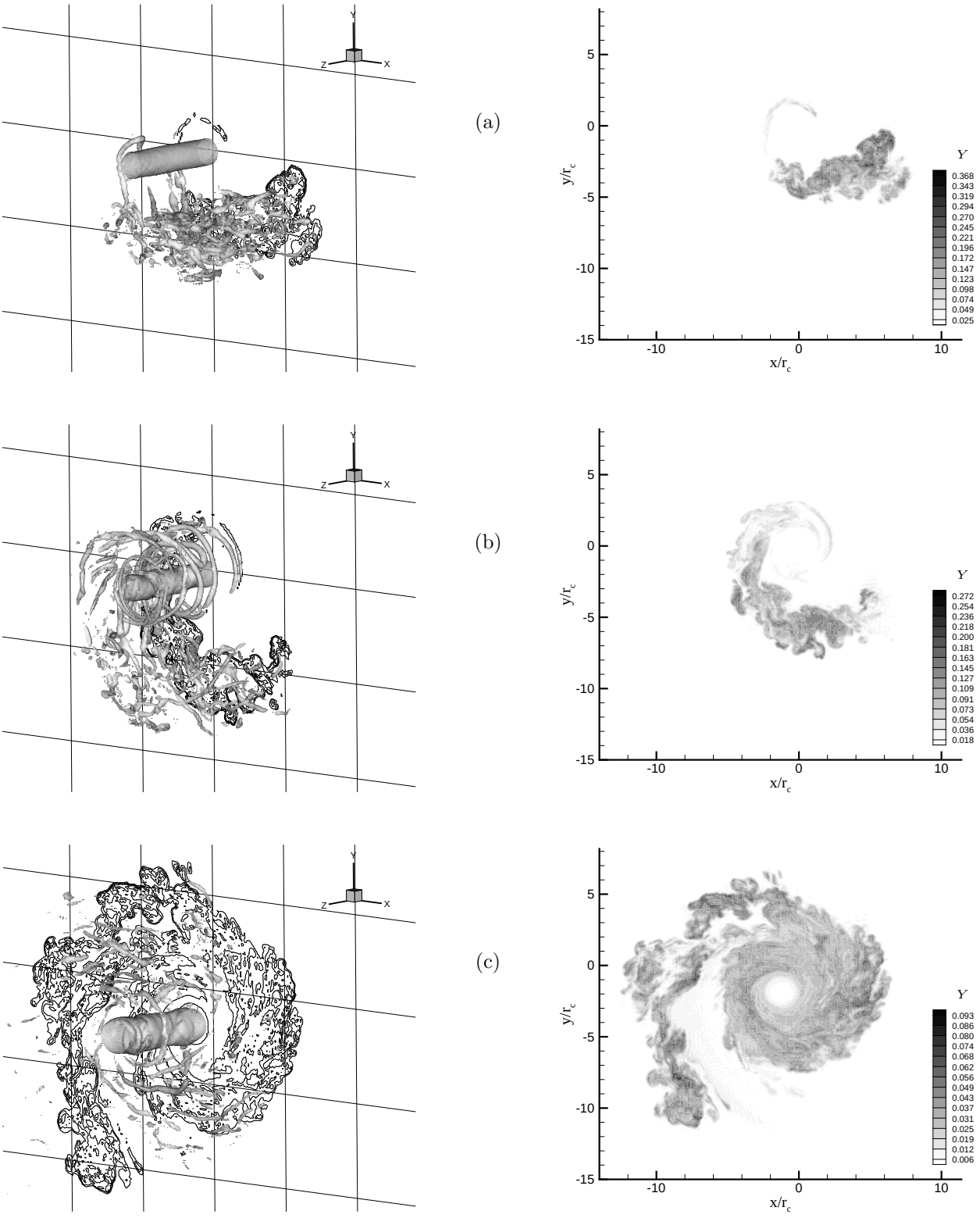

PHYS. FLUIDS – figure 10

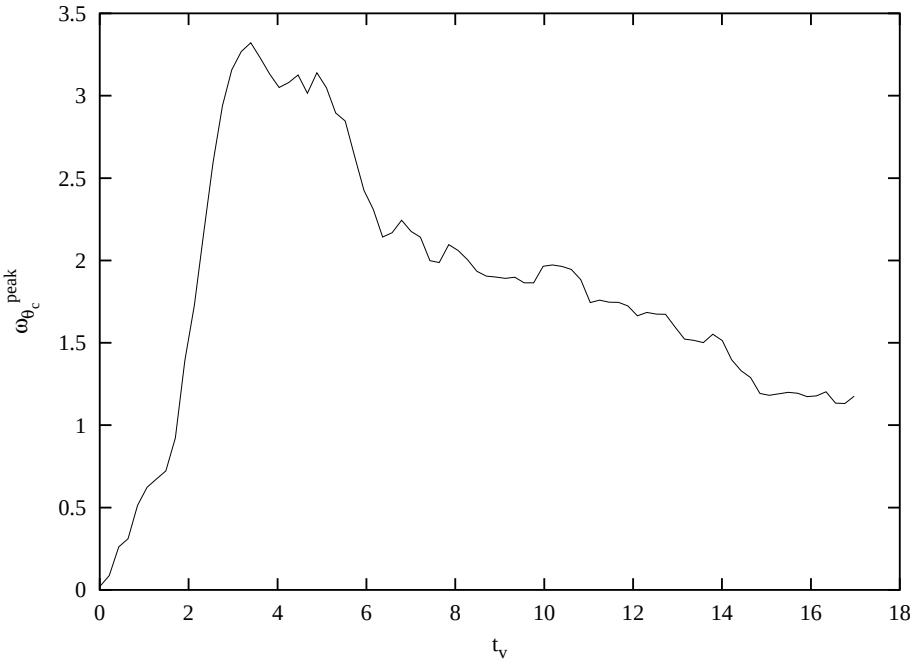

PHYS. FLUIDS – figure 11

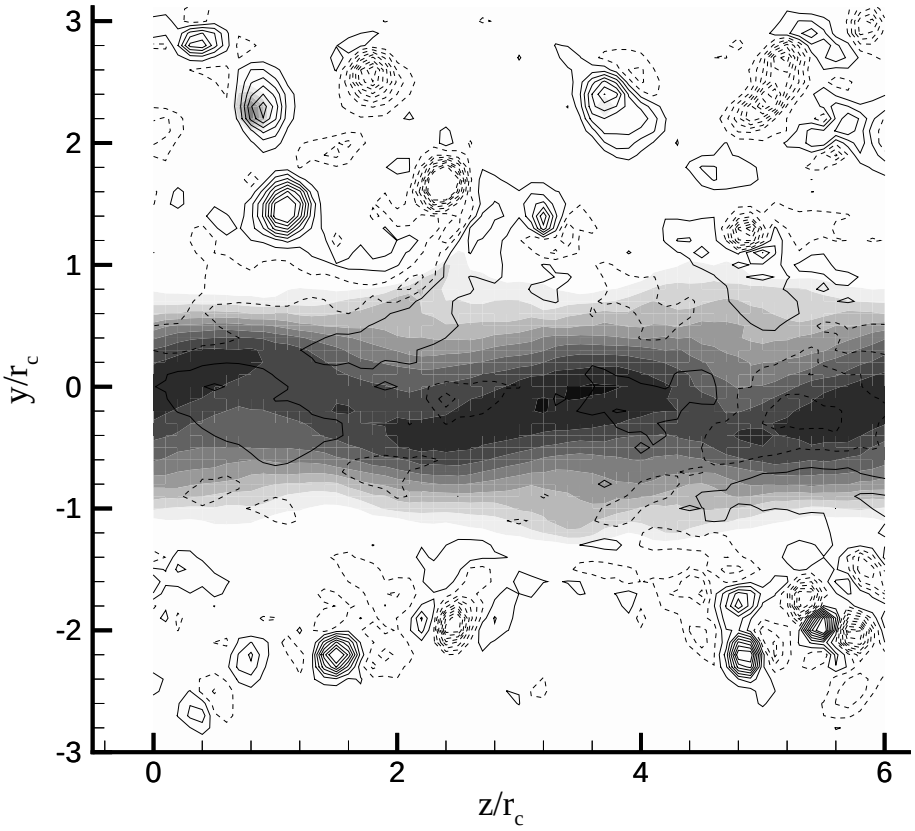

PHYS. FLUIDS – figure 12

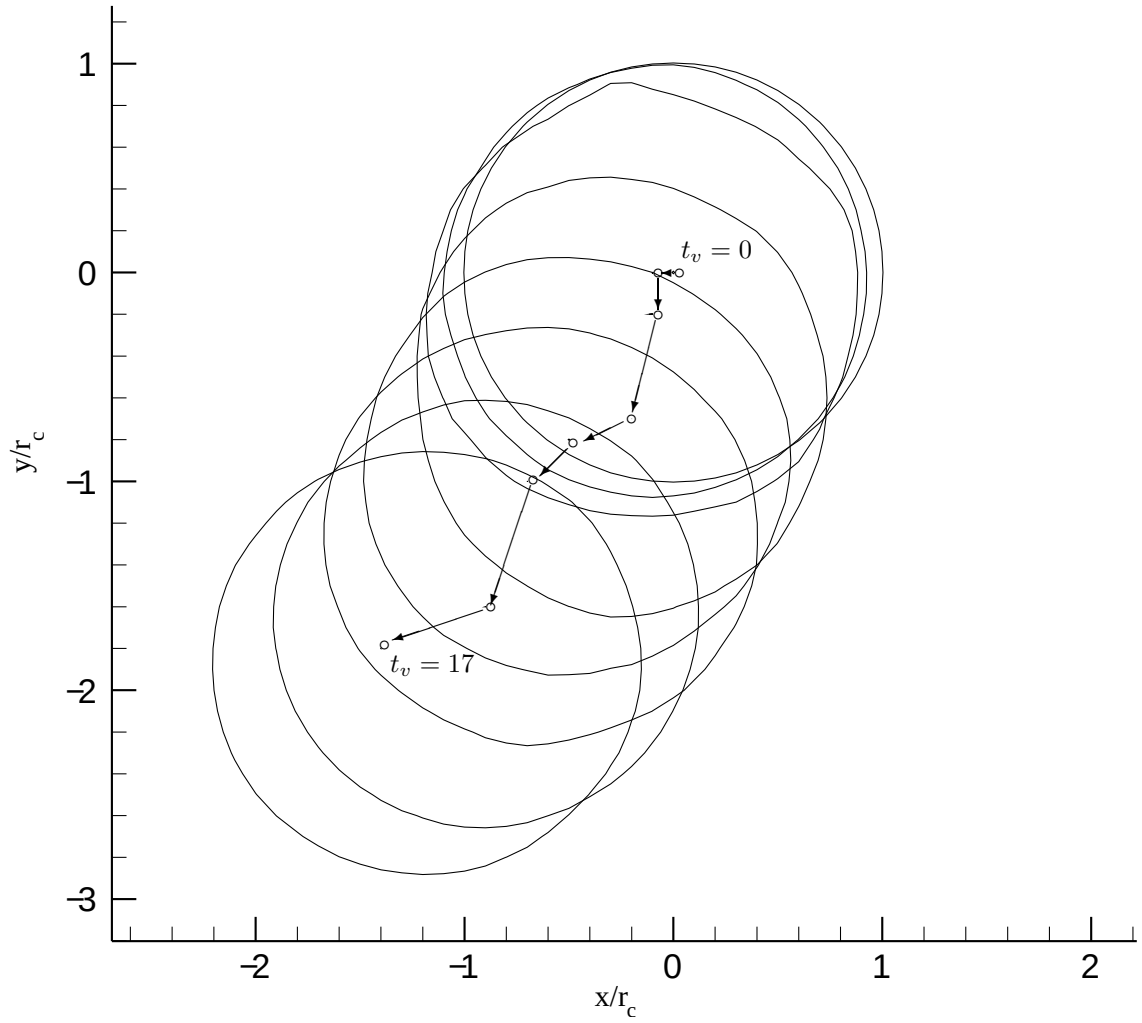

PHYS. FLUIDS – figure 13

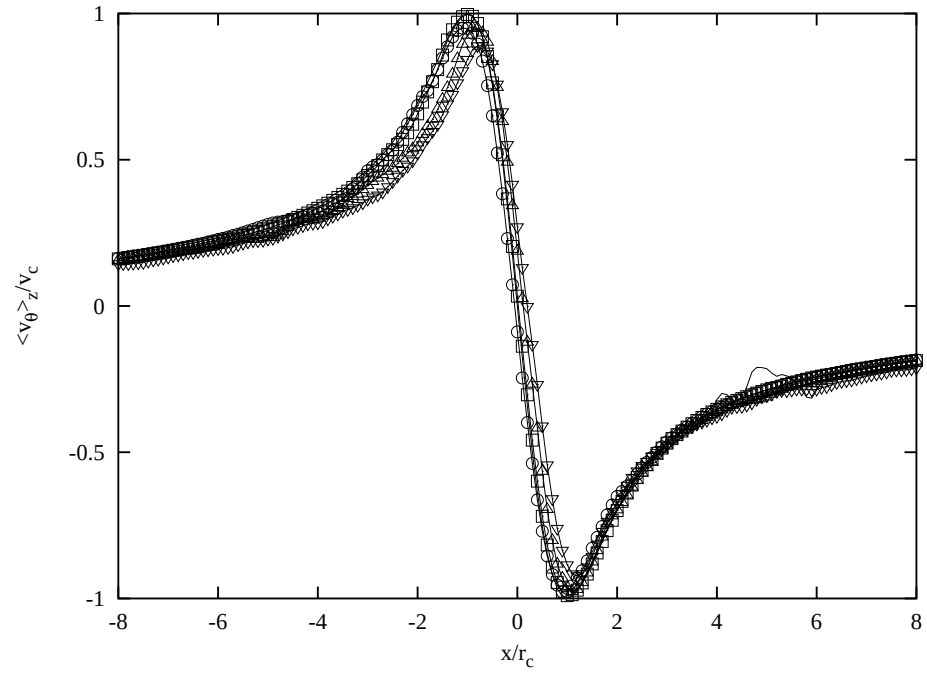
1
0.5
0
-0.5
-1
-8
-6
-4
-2
0
2
4
6
8
<v_θ>/v_c
x/r_c

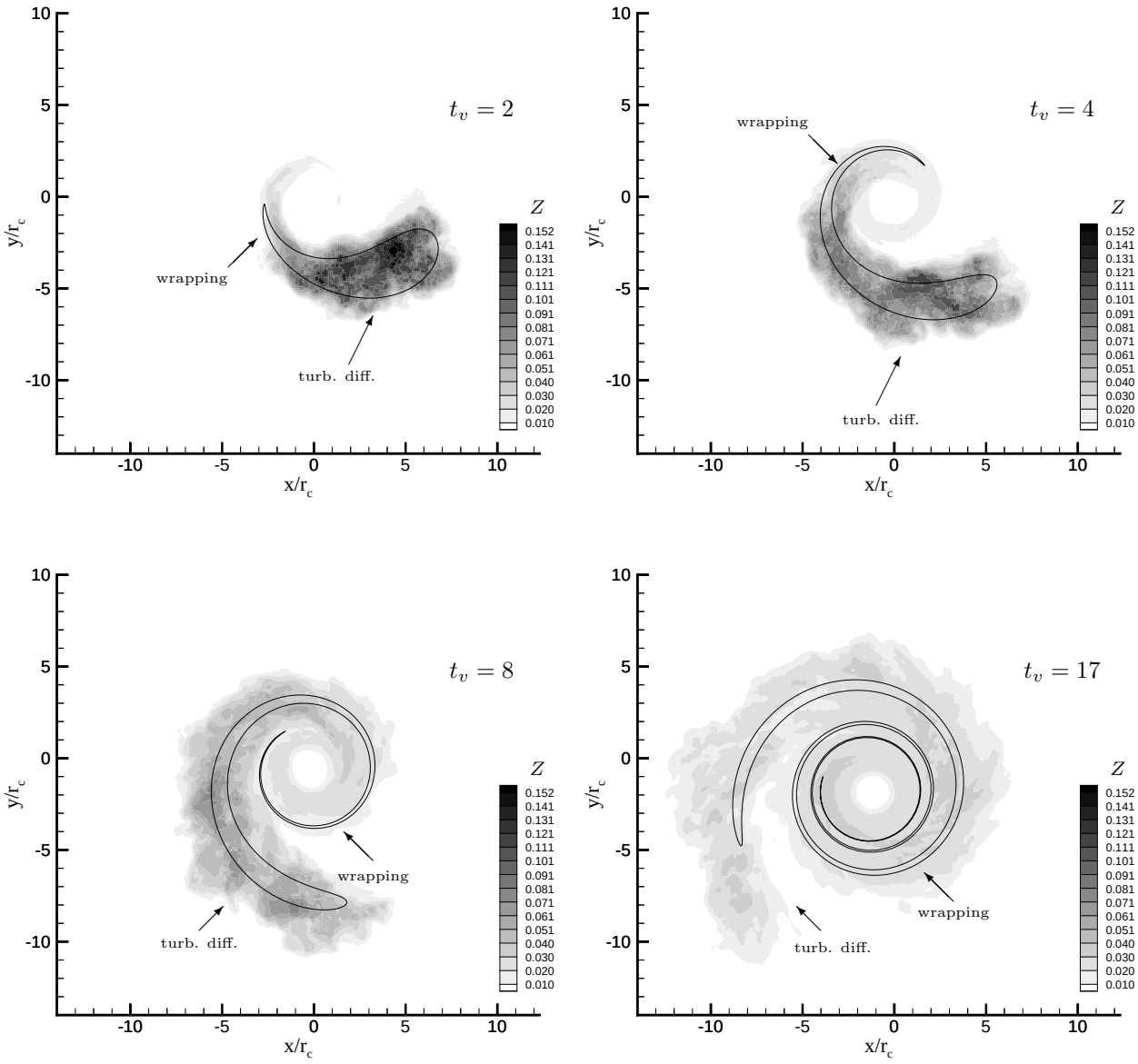

PHYS. FLUIDS – figure 15

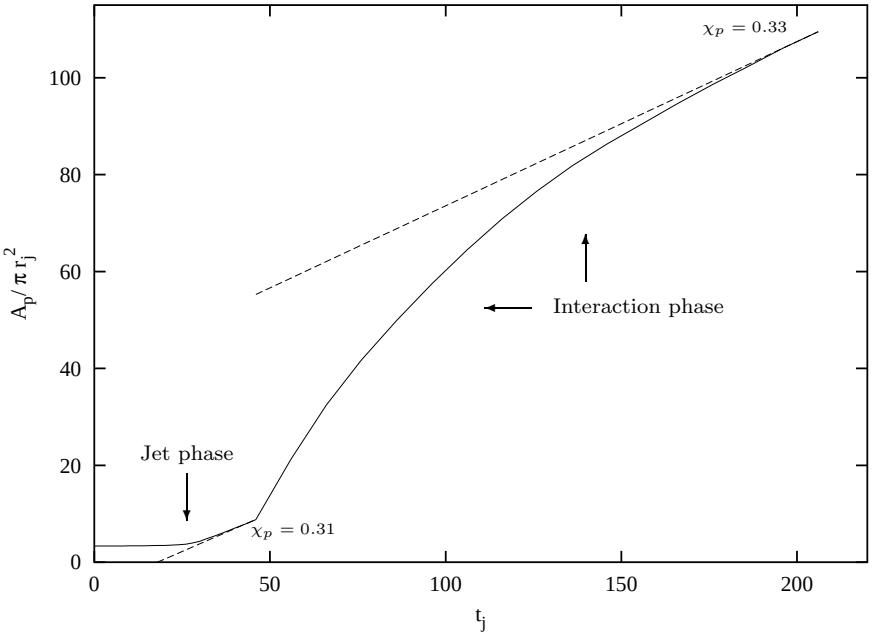

PHYS. FLUIDS – figure 16

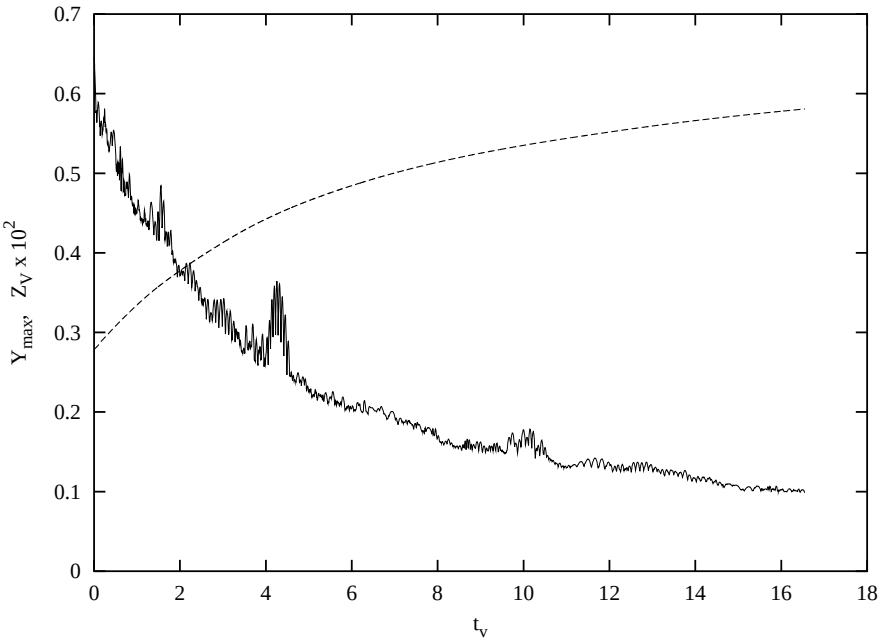

PHYS. FLUIDS – figure 17

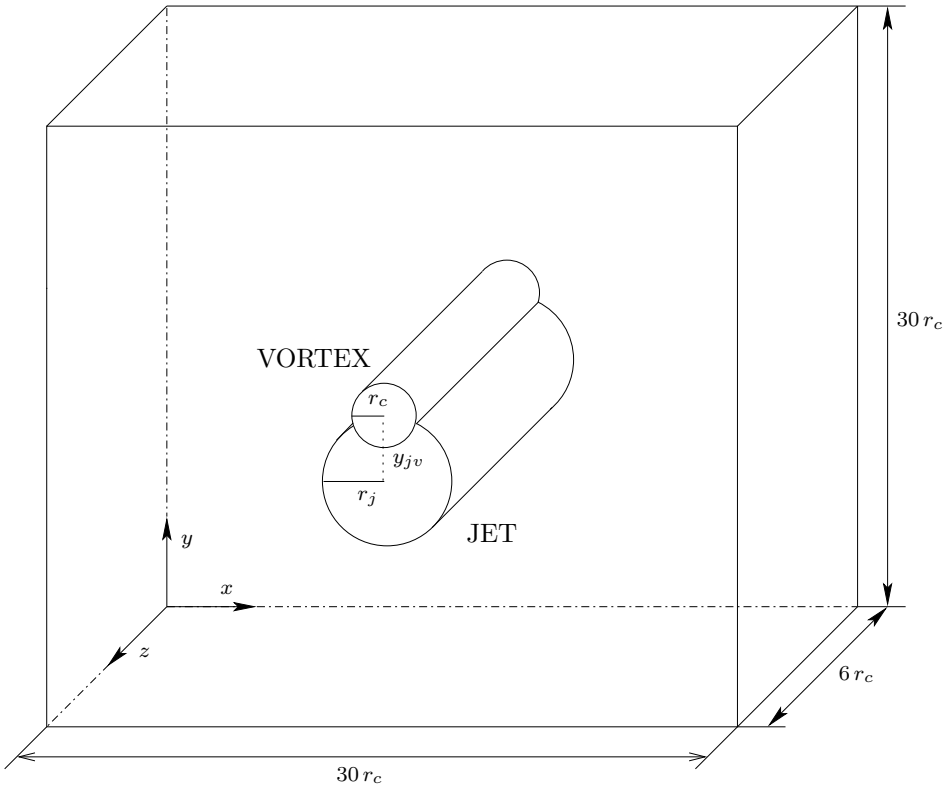

PHYS. FLUIDS – figure 18

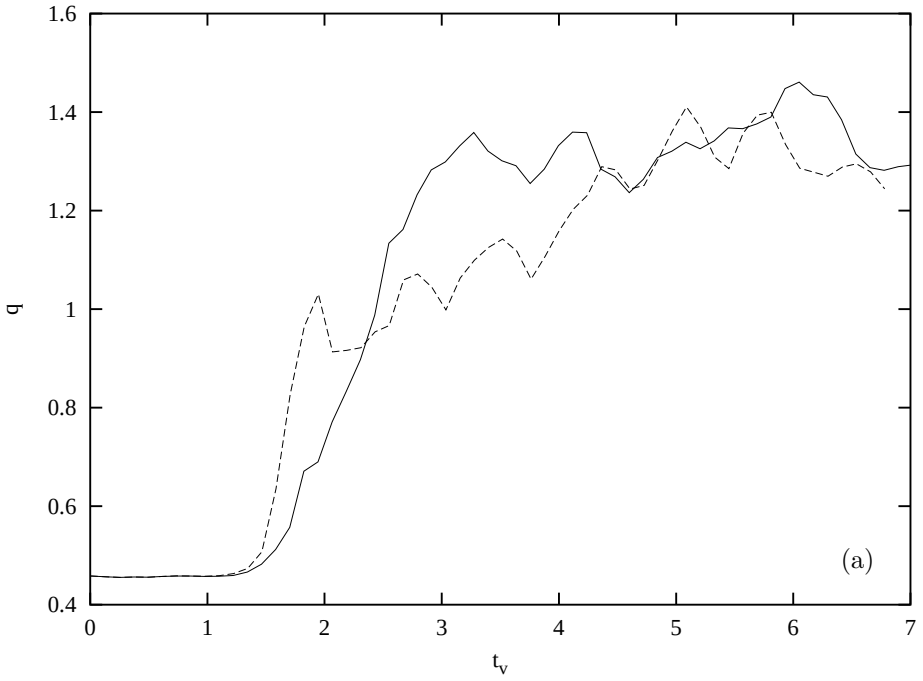

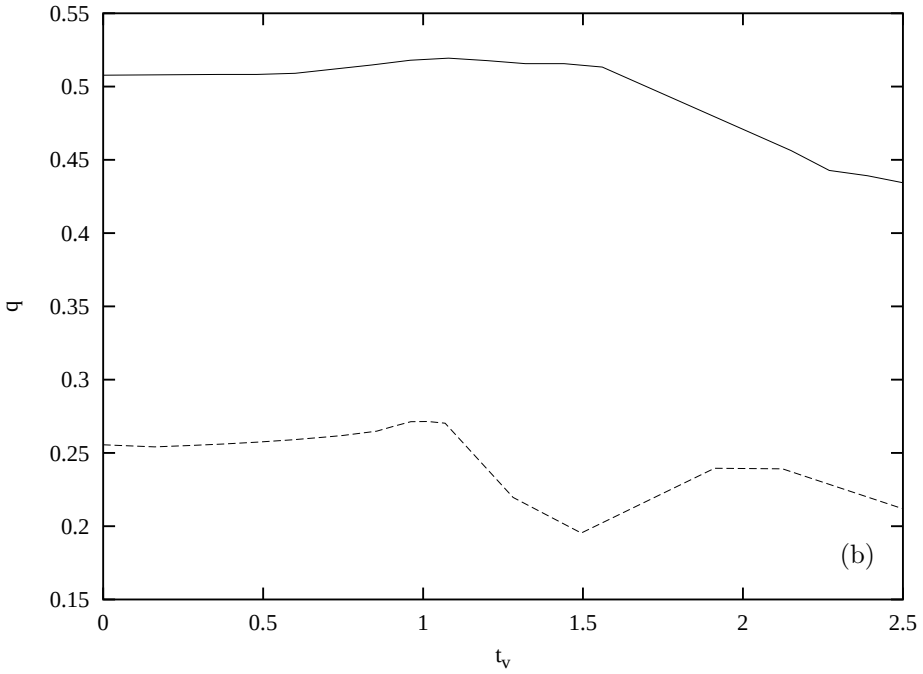

PHYS. FLUIDS – figure 19

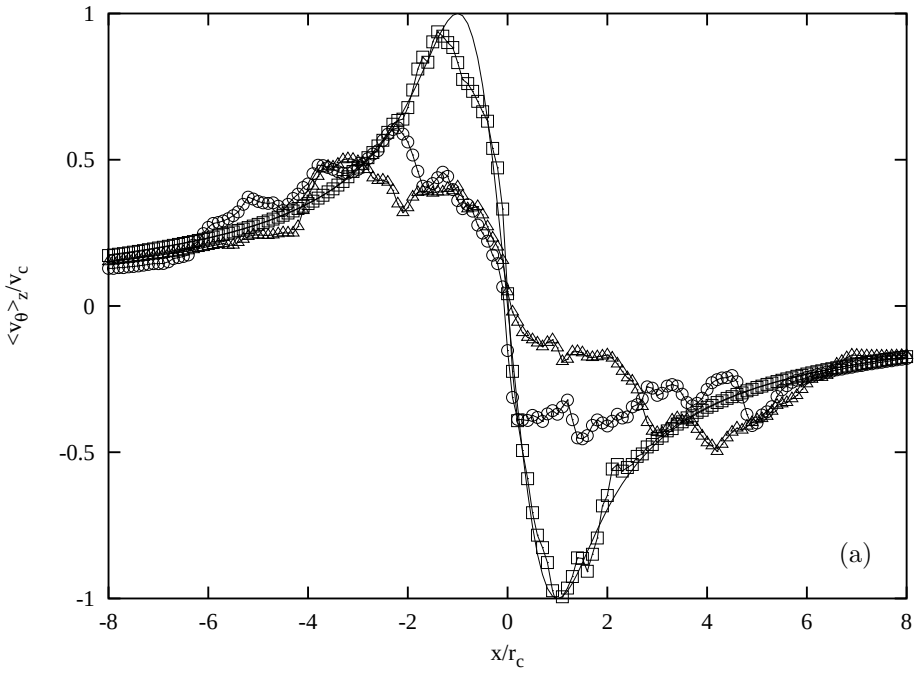

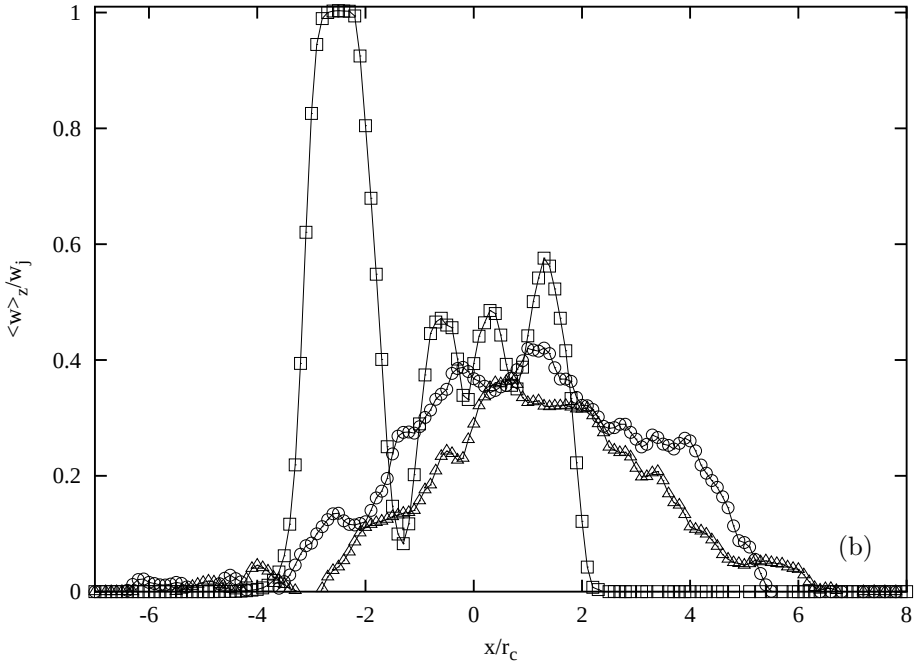

PHYS. FLUIDS – figure 20

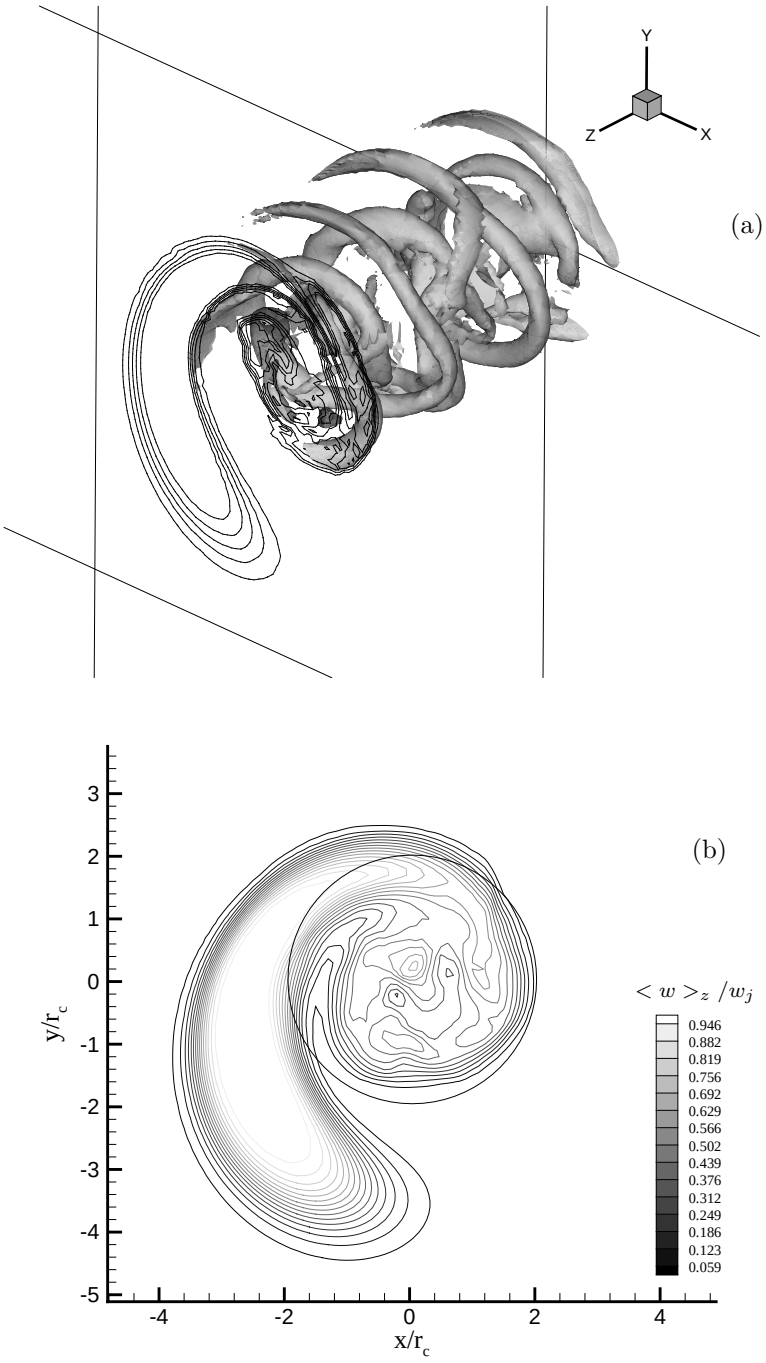

PHYS. FLUIDS – figure 21

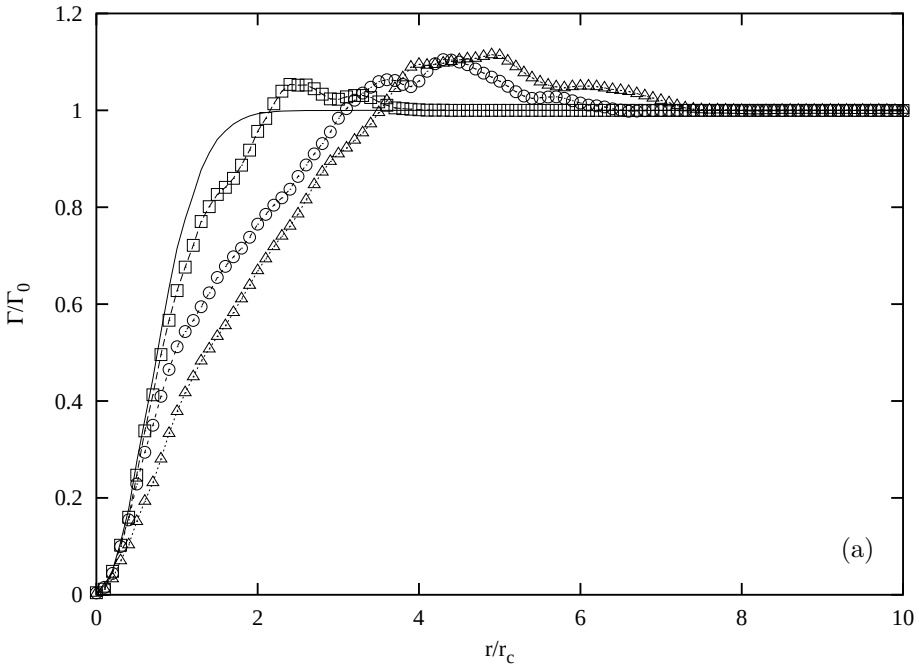

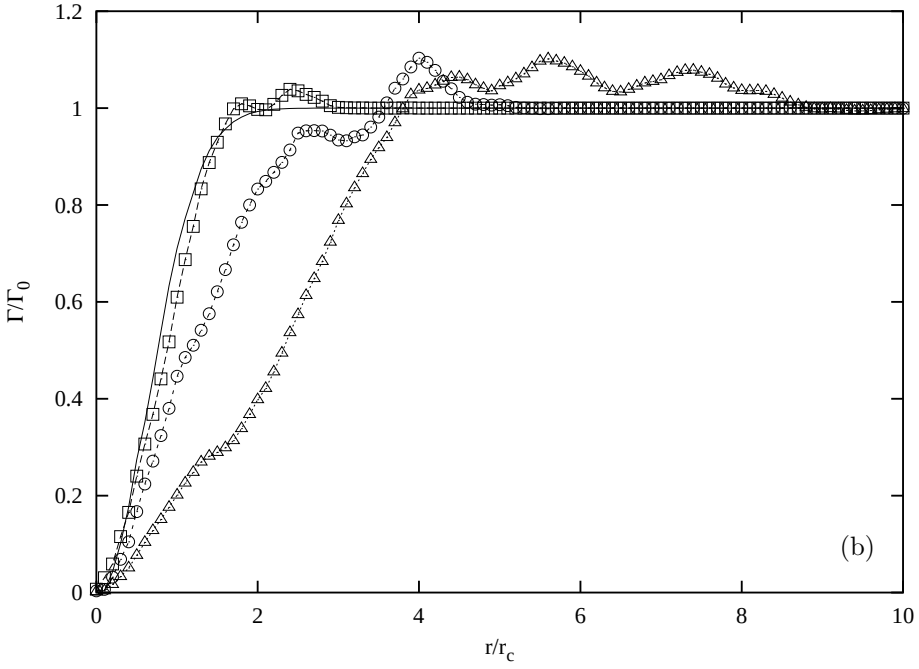

PHYS. FLUIDS – figure 22

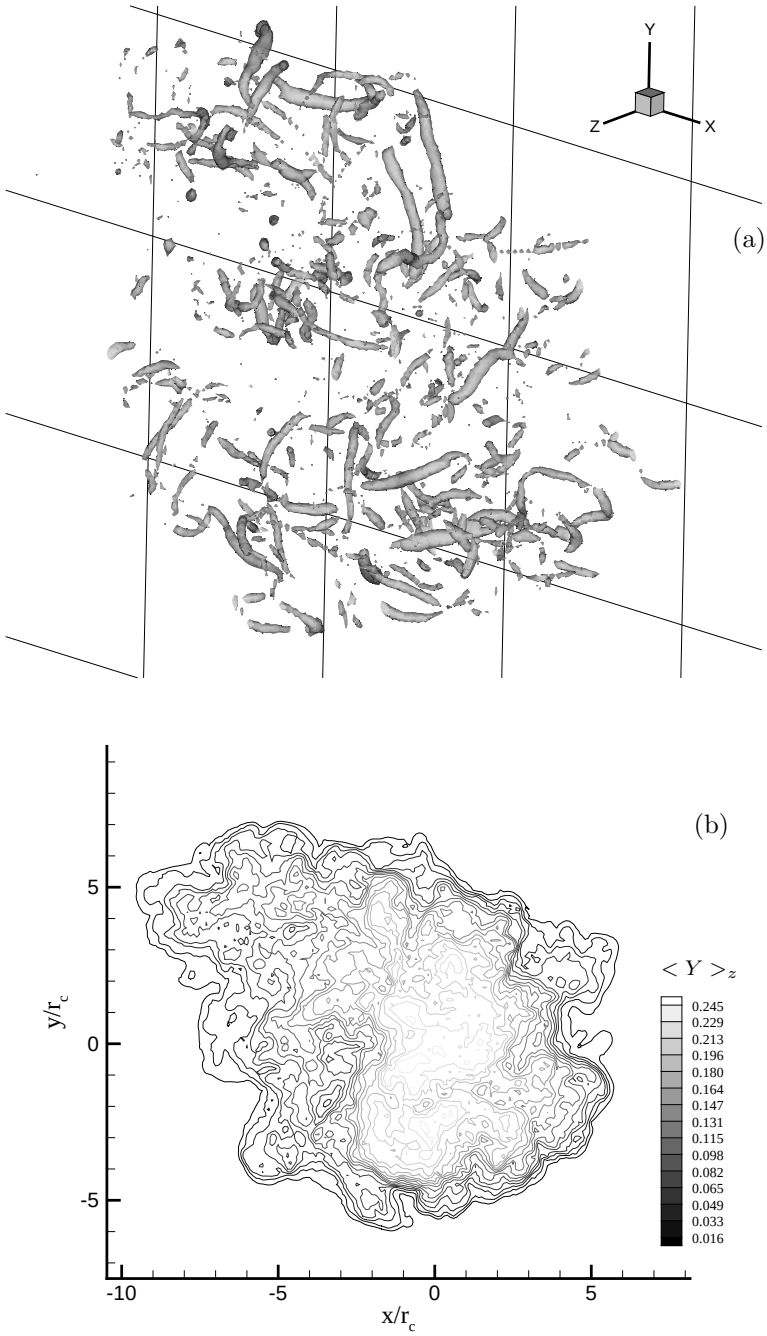

PHYS. FLUIDS – figure 23

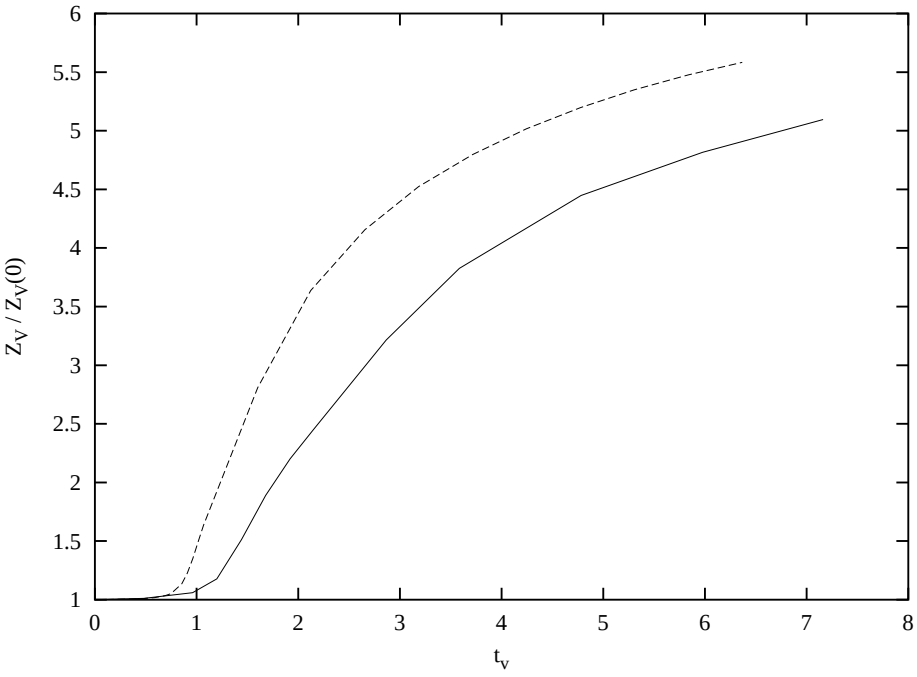

PHYS. FLUIDS – figure 24

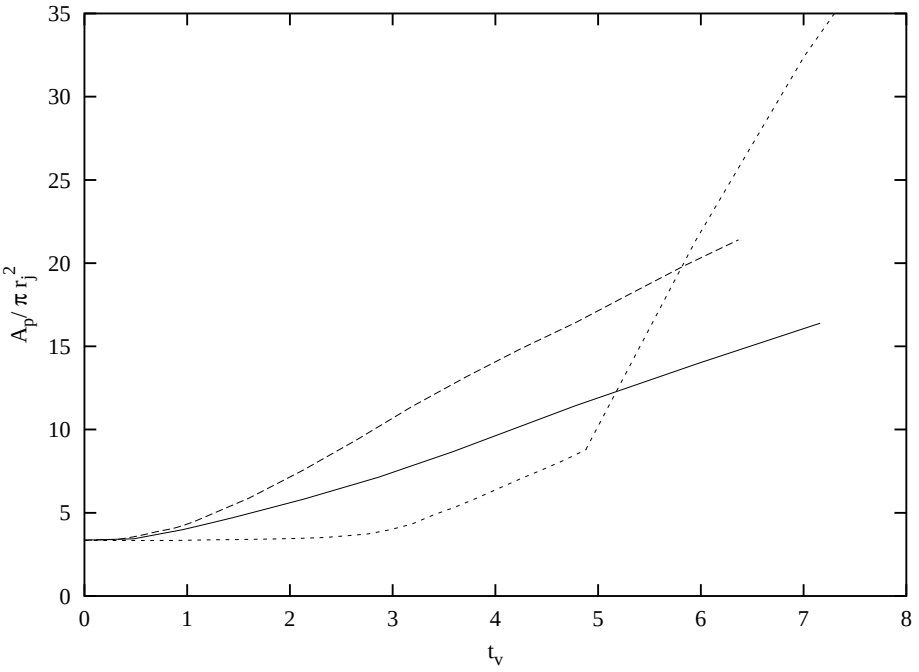

PHYS. FLUIDS – figure 25

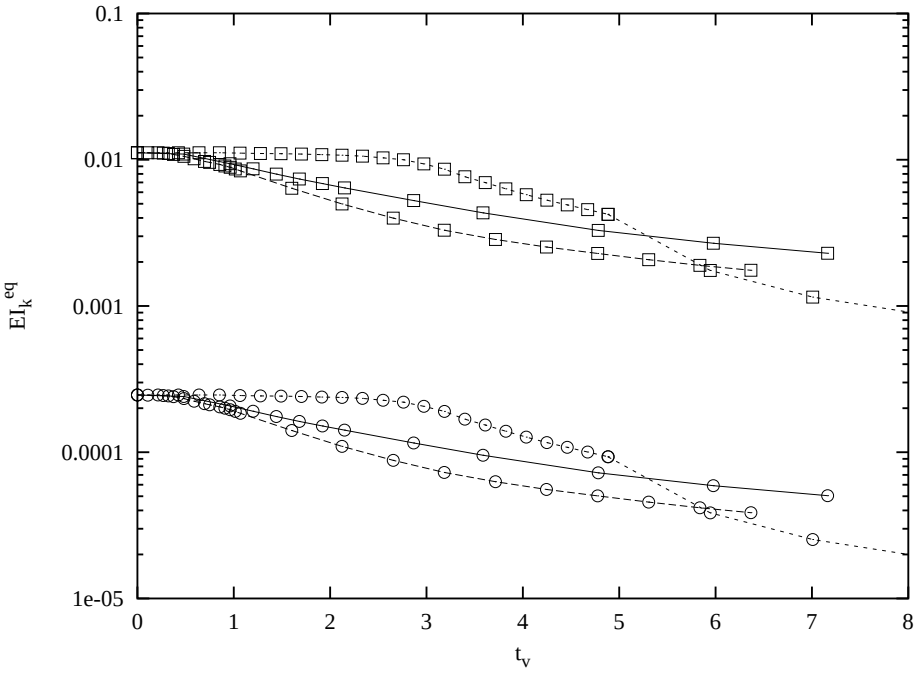

PHYS. FLUIDS – figure 26

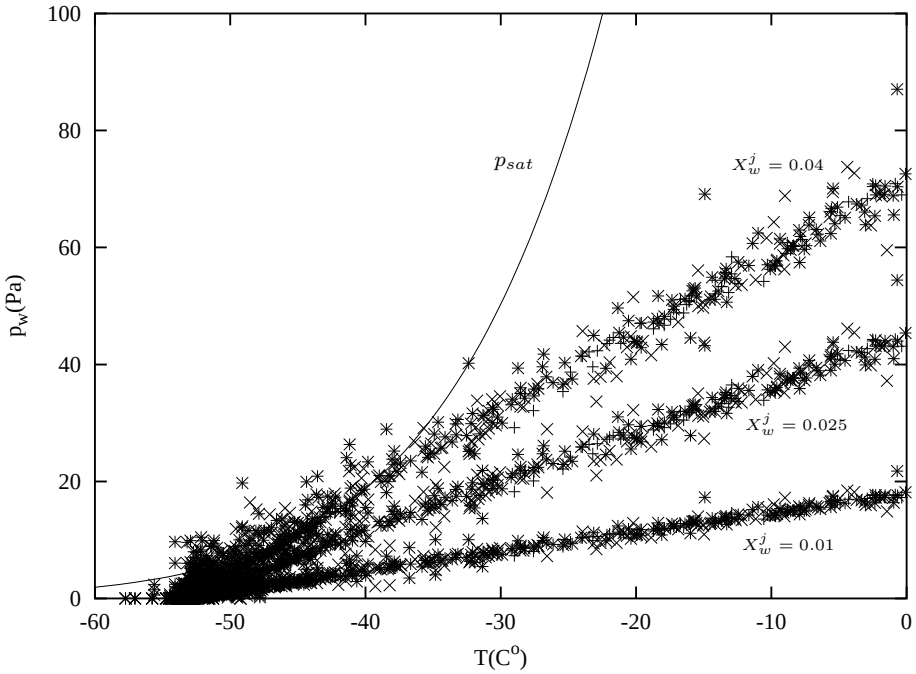

PHYS. FLUIDS – figure 27